

Physicochemical and biological properties of nanohydroxyapatite grafted with star-shaped poly(ϵ -caprolactone)

Eleni Cristina Kairalla, José Carlos Bressiani, Ana Helena de Almeida Bressiani, Maria Tereza de Carvalho Pinto Ribela, Olga Zazuco Higa & Alvaro Antonio Alencar de Queiroz

To cite this article: Eleni Cristina Kairalla, José Carlos Bressiani, Ana Helena de Almeida Bressiani, Maria Tereza de Carvalho Pinto Ribela, Olga Zazuco Higa & Alvaro Antonio Alencar de Queiroz (2022) Physicochemical and biological properties of nanohydroxyapatite grafted with star-shaped poly(ϵ -caprolactone), Journal of Biomaterials Science, Polymer Edition, 33:18, 2353-2384, DOI: [10.1080/09205063.2022.2104599](https://doi.org/10.1080/09205063.2022.2104599)

To link to this article: <https://doi.org/10.1080/09205063.2022.2104599>



Published online: 01 Aug 2022.



Submit your article to this journal [↗](#)



Article views: 60




View related articles [↗](#)



View Crossmark data [↗](#)



Physicochemical and biological properties of nanohydroxyapatite grafted with star-shaped poly(ϵ -caprolactone)

Eleni Cristina Kairalla, José Carlos Bressiani, Ana Helena de Almeida Bressiani, Maria Tereza de Carvalho Pinto Ribela, Olga Zazuco Higa and Alvaro Antonio Alencar de Queiroz 

Centro de Biotecnologia - CEBIO, Instituto de Pesquisas Energéticas e Nucleares (IPEN), São Paulo, SP, Brazil

ABSTRACT

To overcome the disadvantages generated by the lack of interfacial bonding between hydroxyapatite nanocrystals (HAPN) and agglomeration of particles in the development of biodegradable nanocomposites a chemical grafting method was applied to modify the surface of HAPN through grafting of the three-arms star-shaped poly(ϵ -caprolactone) (SPCL) onto the nanoparticles. The chemical grafting of SPCL onto HAPN (SPCL-g-HAPN) has been investigated using Fourier transform infrared spectroscopy, thermogravimetric analysis, transmission electron microscopy (TEM), photoelectron spectroscopy, X-ray diffraction, zeta potential (ZP) and contact angle (CA). TEM micrographs of the SPCL-g-HAPN revealed the existence of hybrid organic/inorganic (O/I) nanoscale domains. The results of albumin (HSA) and fibrinogen (HFb) adsorption indicate resistance to HFb adsorption by SPCL-g-HAPN relatively to unmodified HAPN. The ZP and CA measurement suggest a heterogeneous topology for SPCL-g-HAPN likely due to the existence of hydrophobic-hydrophilic regions on the nanocomposite surface. The enzyme degradation by cholesterol esterase and lipase indicates that the rates of hydrolysis for SPCL-g-HAPN were very slow relative to the SPCL/HAPN blends. The *in vitro* biological studies showed that the human osteoblast-like cells (MG-63) cells had normal morphology and they were able to attach and spread out on SPCL-g-HAPN surfaces. A higher overall cellular proliferation was observed on SPCL-g-HAPN scaffolds compared to pure HAPN or SPCL materials.

ARTICLE HISTORY



Received 21 May 2022
Accepted 19 July 2022

KEYWORDS

Hydroxyapatite nanocrystals; star-shaped poly(ϵ -caprolactone); nanocomposites; protein adsorption; biodegradability; MG-63 cell adhesion

1. Introduction

The integration between the human biological organism and synthetic materials provided by contemporary science has led to a large increase in life expectancy; much

CONTACT Alvaro Antonio Alencar de Queiroz  alvaro.queiroz@ipen.br; dealenquer@gmail.com  Instituto de Pesquisas Energéticas e Nucleares (IPEN), Av. Lineu Prestes 2242, Cidade Universitária, CEP: 05508-000 São Paulo, SP, Brazil.

further than imagined by the Roman Empire where the average life expectancy was about 40 years [1]. However, human being faces aging, the progressive deterioration of biological tissues and organs after nearly four or five decades of existence. The development of surgical procedures for the deployment of new organs or tissues and the evolution of manufacturing 3D prototyping processes from synthetic materials based on the mimicry of the biological tissue is a routine in this century.

Mimicking the biological tissue for the synthesis of biomaterials has been the focus of researchers for many decades. Several efforts have been employed for the design and synthesis of innovative biomaterials and devices for regenerative medicine based on biomimetics of biological tissue [2–4]. Today, contemporaneous biomaterials are highly organized structures from the molecular to the nanoscales hierarchically with intricate nanoarchitectures that ultimately make up a myriad of different biofunctional soft and hard tissues [5, 6].

Advancements in nanotechnology techniques have allowed biomaterials researchers to work at the atomic and molecular levels matching the working scale of a living cell providing platforms and biomimetic devices that can be used for bottom-up construction of synthetic nanosystems with cell-like characteristics [7, 8]. Nanotechnologies that allow a ‘bottom-up’ approach can supply useful tools for the synthesis of innovative biomaterials, mimicking nature not only in composition but also in size, morphology, structure and surface bioactivity.

The past three decades have witnessed a tremendous increase in the use of hydroxyapatite (HAP) in the manufacture of scaffolds for tissue engineering [9, 10]. Surface charges of HAP are recognized as one of the important factors in determining their biological responses. The effect of the surface charges is directly propagated to cells as well as indirectly *via* ionic and macromolecular substances adsorbed onto HAP [11]. In particular, HAP has prominent effects on the proliferation of osteoblastic cells [12] and has reconstructive interaction with bone tissue [13]. Although the effects of the charges on HAP surface still are controversial, both negative and positive charges influenced biological cell activities on its surfaces [14, 15].

Today it is well known that the resorption process of HAP is quite different from that of bone minerals. Bone mineral crystals are nanosized with a very large surface area and higher bioactivity compared with microsized HAP [16]. The nanosized HAP of bone crystals grown in an organic collagen matrix have very loose crystal-to-crystal bonds and show higher bioactivity compared with strong crystal-to-crystal bonds microsized HAP [17]. For this reason, engineered hydroxyapatite nanocrystals (HAPN) grown *in situ* in organic polymeric matrixes would have superior functional properties due to their grain size, large surface area to volume ratio, and crystallinity similar to bone HAP.

During the last three decades, scaffolds to support bone regeneration based on HAPN and biodegradable polymer composites have been extensively developed for bone tissue engineering applications for availing better mechanical properties and bone regeneration capabilities [18–20]. It is well known that ceramic materials based on HAPN are bioinert while bioactive and biodegradable polymer matrices tend to be mechanically weak when produced with a large volume fraction of porosity [6, 21]. Therefore, combining biodegradability, bioactivity, and mechanical property, a hybrid

organic-inorganic (O/I) matrix composed of biodegradable polymers and HAPN can offer an interesting opportunity to produce biomimetic scaffolds with desired biological, physical, and structural properties. Additionally, from a biological perspective, the constituents of the O/I hybrids matrixes resemble the structure of bone tissue, where the inorganic component mimics the biological ceramic (HAPN) and the polymer component mimics the collagen-rich extracellular matrix.

It is already widespread in the literature that poly(ϵ -caprolactone) (PCL) is one of the most attractive and promising synthetic polymers for applications in regenerative medicine due to their biodegradability, FDA approval and thus, it has potential importance in several different applications in medicine [22, 23].

Over the last years, several studies have analyzed the influence of the HAPN content and the processing route of O/I composites based on PCL for the development of many synthetic bone-like composites and tissue-engineered scaffolds [24, 25]. However, in making PCL-HAPN composites, the lack of interfacial bonding between HAPN and the polymer matrix remains an issue of concern, and studies have shown that the bond strengths in such hybrid materials are difficult to be controlled. The internal interfaces in the microstructures of these composites invariably provide the weakest links for the nucleation of cracks that lead to premature failure in physiological conditions. Additionally, the degradation of the internal interfaces of the HAPN-PCL induced by water seriously compromises the mechanical stability of these composites for real *in vivo* applications [26, 27].

The use of star-shaped poly(ϵ -caprolactone) (SPCL) covalently bound to HAPN surfaces will overcome the problem of the instability of the internal interface between the O/I phases. SPCL and its copolymers have drawn great attention from many researchers for their interesting functional properties for tissue engineering applications [28, 29]. The grafting of SPCL chains onto the HAPN surface (SPCL-g-HAPN) offers an exceptional opportunity to produce scaffolds with desired biological, physical, and structural properties.

It could be emphasized that SPCL-g-HAPN chains will differ from their nanocomposite counterparts where both, inorganic components and the polymer chains interact through chemical bonding at the molecular level. Furthermore, the SPCL-g-HAPN forms a single-phase material, consisting of a homogenous mixture between the organic (SPCL) and inorganic (HAPN) compounds. As such, the intimate nature of the interface in O/I hybrids will result in superior mechanical properties. At the same time, the release of acidic degradation by-products from biodegradable polymers can cause inflammatory reactions, while the basic degradation of HAPN could buffer the acidic by-products avoiding the formation of an unfavorable environment for cells due to the low pH in biological tissue environments.

Recently, it was demonstrated that the interfacial interactions between polymer and HAPN could be greatly enhanced by the direct grafting of linear poly(ϵ -caprolactone) (PCL) onto HAPN [30–32]. In this way, the connection between HAPN and PCL would be strengthened improving uniformity of the ceramic nanoparticles in the composite and better mechanical properties would be obtained. In addition to the grafting method to improve the interaction between polymer matrix and HAPN, the type of polymer molecule and its density after grafting play key roles

in the biological, physical, and structural properties of the composite and mainly depend on PCL chain length and grafting density [33]. In this regard, star-shaped SPCL may be advantageous because of their molecular architecture and long-chain length, which enable higher grafting density than linear PCL. Additionally, SPCL offers a high density of functional groups that allow subsequent grafting of selected biomolecules designed to further tailor surface properties so that is useful for tissue engineering [34].

This work reports a synthetic approach to preparing the SPCL anchored to HAPN through a grafting reaction to obtain SPCL-g-HAPN. The SPCL-g-HAPN was also characterized through physicochemical and biological analysis. Finally, the enzymatic degradation and the interaction of the SPCL-g-HAPN with human serum albumin (HSA), human serum fibrinogen (HFb), and MG-63 cells line are discussed in detail.

2. Experimental

2.1. Materials

All chemicals were used as received from the manufacturer without further purification. Triethylamine (TEA), p-toluenesulfonyl chloride (TsCl), tetraethylene glycol, thioacetic acid (CH_3COSH), sodium hydride (NaH), sodium chloride (NaCl), phosphate-buffered saline solution pH 7.4 (PBS), uranyl acetate (UA), lithium bromide (LiBr), 2,5-dihydroxybenzoic acid (DHB), sodium hydroxide (NaOH), calcium nitrate 4-hydrate ($\text{Ca}(\text{NO}_3)_2 \cdot 4\text{H}_2\text{O}$), diammonium hydrogen phosphate ($(\text{NH}_4)_2\text{HPO}_4$), 3-glycidyloxypropyl trimethoxysilane (GPTMS), ethanol (EtOH), n-hexane (Hex), petroleum ether, chloroform (CHCl_3), dichloromethane (DCM), acetonitrile (ACN), ethyl acetate, dimethylformamide (DMF), dimethylsulfoxide (DMSO), ϵ -caprolactone (ϵ -CL), acetone (ACE), Triton® X-100, (3-[4,5-dimethylthiazol-2-yl]-2,5-diphenyl-2H-tetrazolium bromide) (MTT reagent), polystyrene molecular weight standards (PS), hydrochloric acid (HCl), o-nitrophenyl phosphate, 2,5-dihydroxybenzoic acid (DHB), deuterated chloroform (CDCl_3), tetramethylsilane (TMS), glycerol (Gly) and tin 2-ethyl hexanoate ($\text{Sn}(\text{Oct})_2$) were purchased from Across or Sigma-Aldrich. Human serum albumin (HSA), human serum fibrinogen (HFb), and Sephadex G-25 columns were purchased from Sigma-Aldrich. ^{125}I in form of sodium iodide (NaI^{125}) was purchased from Amersham (IMS-30, New England Nuclear, Boston). Sodium thioacetate (NaSAc) was synthesized in our laboratories immediately before use by reacting CH_3COSH with NaH under an argon atmosphere (Ar). Liquid Ar, nitrogen (N_2) and carbon dioxide (CO_2) gases, with 99.999% of purity, were provided by White Martins (São Paulo, SP, Brazil). Human osteoblast-like cells of the line MG-63 were purchased from American Type Culture Collection-ATCC, CRL-1427 (EUA). Dulbecco's modified Eagle medium (DMEM), fetal bovine serum (FBS), penicillin (PCN) and streptomycin (STM) were purchased from Gibco, Thermo Fisher Scientific, Inc. Formaldehyde (FD), fluorescein isothiocyanate-phalloidin conjugate (FITC-PHN), acridine orange (AO) and ethidium bromide (EtBr) were purchased from Sigma-Aldrich (Brazil). Plysurf A210G was acquired from Daiichi Kogyo Seiyaku (Japan). Lipase (LIPH, EC 3.1.1.3), cholesterol esterase (CHE, EC 3.1.1.13) and o-nitrophenyl phosphate (o-NPP) were purchased from; Sigma-Aldrich (SP, Brazil).

2.2. Characterization techniques

^1H - and ^{13}C -NMR spectra of all compounds synthesized in this work were obtained on a Bruker FT-NMR spectrometer (400.13 MHz for ^1H and 100.61 MHz for ^{13}C) in CDCl_3 at room temperature (27 °C). TMS was used as an internal reference compound for NMR.

The matrix-assisted laser desorption/ionization (MALDI) experiments were carried out on a Kratos Kompact III spectrometer in the reflection mode, operating with irradiation from a nitrogen laser at 337 nm. Samples were prepared by first laying down 0.5 μL of a 10^{-1} mol dm^{-3} solution of DHB in 50% water–50% CHCl_3 , followed by 0.5 μL of a 10^{-3} mol dm^{-3} solution of 2 in 50% water–50% CHCl_3 . Spectra were averaged over 200 laser pulses while scanning across the sample. Samples were doped with sufficient NaCl to simplify the spectra by suppression of the $\text{M} + \text{K}^+$ peaks. Hence, all molecular ions are observed as $\text{M} + \text{Na}^+$ peaks.

Absolute weight (M_w) and the number of average molecular weights (M_n) of SPCL were determined by size exclusion chromatography (SEC) using a Waters 1525 pump (Waters, Milford, MA) equipped with a differential refractive index detector (Waters 2410) and PD 2000 light scattering detector (Precision Detectors, Franklin, MA). Three columns HT2, HT3, and HT4 with a very high to low molecular weight separation range were used in series. SPCL samples were dissolved in DMF (4 mg mL^{-1}) and injected into the system. The mobile phase was DMF containing 10 mmol LiBr. Flow rate and temperature were set at 1.0 mL min^{-1} and room temperature (27 °C). PS (0.25–65 kDa) were used to calibrate the column system.

The elemental phase composition of the HAPN powder was analyzed using X-ray photoelectron spectroscopy (XPS). XPS measurements were performed on the dried powder HAPN and SPCL-g-HAPN with a Kratos AXIS Ultra photoelectron spectrometer. The dried powder of SPCL-g-HAPN was thoroughly washed with DCM in a Soxhlet extractor for 48 h to remove some physically adsorbed SPCL homopolymer and then kept in a vacuum oven at 60 °C overnight before analysis. The XPS experiments were conducted at room temperature (25 °C) with a base pressure of 1.10^{-9} bar. The monochromatic AlK_{α} -X-ray source was operated at 300 W (15 kV, 20 mA). The low-resolution survey scans were taken with a 1 eV step and 80 eV analyzer pass energy; high-resolution spectra were taken with a 0.1 eV step and 20 eV analyzer pass energy. Quantitative XPS analyses were performed with the Kratos Vision software (version 2.1.2). The atomic concentrations were calculated from the photoelectron peak areas by using Gaussian–Lorentzian deconvolution. The chemical shifts were taken from the literature and the spectra were charge corrected by setting the carbon without oxygen bond contribution in the C_{1s} emission at 285.0 eV.

The X-ray diffraction (XRD) pattern of the SPCL, HAPN, and SPCL-g-HAPN were obtained with $\text{CuK}\alpha$ radiation ($\lambda = 1.5418 \text{ \AA}$) on a D8 Advance (Bruker-AXS, Germany) diffractometer and then analyzed using Ni-filtered $\text{CuK}\alpha$ radiation ($\lambda = 0.1542 \text{ nm}$), in the step scanning mode, with a tube voltage of 40 kV and tube current of 50 mA. The XRD patterns were recorded in the 2θ range of 20°–60°, with a step size of 0.02° and step duration of 0.5 s. The fraction of crystalline phase (X_c) of the HAPN powders was evaluated by the following equation [35]:

$$X_c = \frac{1 - \nu_{112/300}}{I_{300}} \quad (1)$$

where I_{300} is the intensity of (3 0 0) diffraction peak and $\nu_{112/300}$ is the intensity of the hollow between (1 1 2) and (3 0 0) diffraction peaks of HAPN.

Zeta-potential (ZP) experiments were carried out on a Zetasizer 2000 (Malvern Instruments) using a standard rectangular quartz cell. Titrations were done in a 10 mM PBS solution at room temperature (25 °C).

For transmission electron microscopy (TEM), drops of aqueous dispersions of unmodified HAPN (0.01% w/v) and SPCL-g-HAPN were deposited on carbon-coated electron microscope grids (Protochips Inc.), negatively stained with UA and allowed to dry. The samples were analyzed with a Hitachi HF-2000 TEM operated at an accelerating voltage of 80 kV.

2.3. Synthesis of thiolated SPCL

2.3.1. Synthesis of three arms SPCL

Two grams of ϵ -CL (17.5 mmol), 0.03 g of Gly (0.33 mmol) and 0.025 g of Sn(Oct)₂ (0.062 mmol) were placed in a Schlenk polymerization tube equipped with a magnetic stirring bar. The vacuum was applied to the tube for 10 min. Then, the tube was purged with Ar. This procedure was repeated three times. Finally, the tube was closed under vacuum and immersed in an oil bath preheated to 150 °C. Polymerization was allowed to proceed for 24 h under a stirring and Ar atmosphere. The polymerization tube was cooled to room temperature (25 °C) and the resultant SPCL was dissolved in 50 mL of DCM and precipitated in Hex. SPCL (1) was isolated by filtration and dried in a vacuum for 48 h. Yield: 1.70 g (85%). ¹H-NMR selected δ (ppm): 4.01 (2H, t, -CH₂CH₂OC(O)-), 3.70 (2H, t, -CH₂CH₂OH, end group), 2.24 (2H, t, -CH₂CH₂COO-), 1.58 (4H, m, -CH₂CH₂COO-), 1.33 (2H, m, -CH₂CH₂CH₂CH₂CH₂-). ¹³C-NMR selected δ (ppm): 173.1 (-C(O)O-), 63.7 (-CH₂CH₂OC(O)-), 33.6 (-CH₂CH₂COO-), 27.9 (-CH₂CH₂OC(O)-), 25.1 (-CH₂CH₂COO-), 24.1 (-CH₂CH₂CH₂CH₂CH₂-). Fourier transform infrared spectroscopy (FTIR) selected data (ν/cm^{-1}): 2943 ($\nu_{\text{as}}\text{CH}_2$), 2862 ($\nu_{\text{s}}\text{CH}_2$), 1721 ($\nu\text{C}=\text{O}$), 1291 (C-O and C-C) 1240 ($\nu_{\text{as}}\text{COC}$), 1190 ($\nu\text{OC}-\text{O}$), 1170 ($\nu_{\text{s}}\text{COC}$), 1157 (C-O and C-C). GPC data: $M_w = 8280$; $M_n = 5430$; $M_w/M_n = 1.53$.

2.3.2. Synthesis of SPCL tosylate

The tosylant agent TsCl (0.05 mol, 9.82 g) in 100 mL of DCM was added dropwise to a mixture of 0.05 mol (9.71 g) of SPCL (1) and 0.05 mol (5.06 g, 3.67 mL) of TEA over 1 h at 0 °C. The mixture was then stirred overnight at room temperature (25 °C). A white TEA hydrochloride precipitate was filtered off and washed with 50 mL of DCM. DCM was removed under reduced pressure to leave pale yellow oil, which was purified by flash chromatography on silica using DCM and ACN (3:1, 1:1, and 0:1 v/v), to give a 65% yield for tosylated SPCL (SPCL-Ts) (2). Elemental analysis (ThermoScientific, FlashSmartThermo): C = 82.18%, H = 7.56%, and S = 10.22%) and degree of substitution (DS) of 1.02 (based on sulfur analysis). ATR-FTIR select data (ν/cm^{-1}): 810 ($\nu_{\text{s}}\text{S}-\text{O}-\text{C}$), 1180 ($\nu_{\text{s}}\text{SO}_2$), 1360 ($\nu_{\text{as}}\text{SO}_2$) and 1600 ($\nu\text{C}=\text{C}_{\text{aromatic}}$). ¹H-NMR selected δ (ppm): 2.45 (3H, s, CH₃), 7.40 (2H, d, *m*-SO₂C₆H₄), 7.80 (d, *o*-

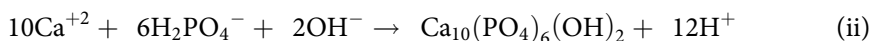
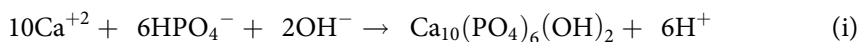
SO₂C₆H₄). ¹³C-NMR selected δ (ppm): 145.5, 132.5, 130.5, 128.2 (C_{aromatic}), and 21.6 ppm (methyl of tosyl group).

2.3.3. Synthesis of mercapto-SPCL

A 0.03 mol portion of SPCL-Ts (2) (10.45 g) in dry ACN (20 mL) was added dropwise over 30 min to 0.036 mol of freshly prepared NaSAc in dry ACN under Ar atmosphere and stirred for 4 h at room temperature (25 °C). The white thioacetyl-SPCL (AcS-SPCL) (3) precipitate was filtered off and the solvent evaporated under reduced pressure. The residue (3) was added to the HCl solution (25 mL, 1 M) and refluxed for 6 h. After solvent evaporation, the residue was purified by flash chromatography on silica using DCM/ACN with 0.1% TEA (3:1, 2:1 and 1:1 v/v). Evaporation of solvents gives 5.44 g of pale yellow solid (86% yields) mercapto-SPCL (HS-SPCL) (4). ¹H NMR selected δ (ppm): 4.01 (2H, t, -CH₂CH₂OC(O)-), 3.70 (2H, t, -CH₂CH₂OH, end group), 2.24 (2H, t, -CH₂CH₂COO-), 1.58 (4H, m, -CH₂CH₂COO⁻), 1.33 (2H, m, -CH₂CH₂CH₂CH₂CH₂-), 2.73–2.68 (m, 2 H, -CH₂S), 1.62 (t, 1 H, SH). Scheme 1 summarizes the synthesis of SPCL (1) and (HS-SPCL) (4).

2.4. Synthesis of HAPN

Aqueous solution of 0.09 M (NH₄)₂HPO₄ and 0.15 M Ca(NO₃)₂·4H₂O were prepared and the pH of both solutions was brought to about 11.0, by adding 1 M NaOH. The (NH₄)₂HPO₄ solution was added dropwise into the Ca(NO₃)₂ solution, resulting in the precipitation of HAPN according to reactions (i) and/or (ii) [36]:

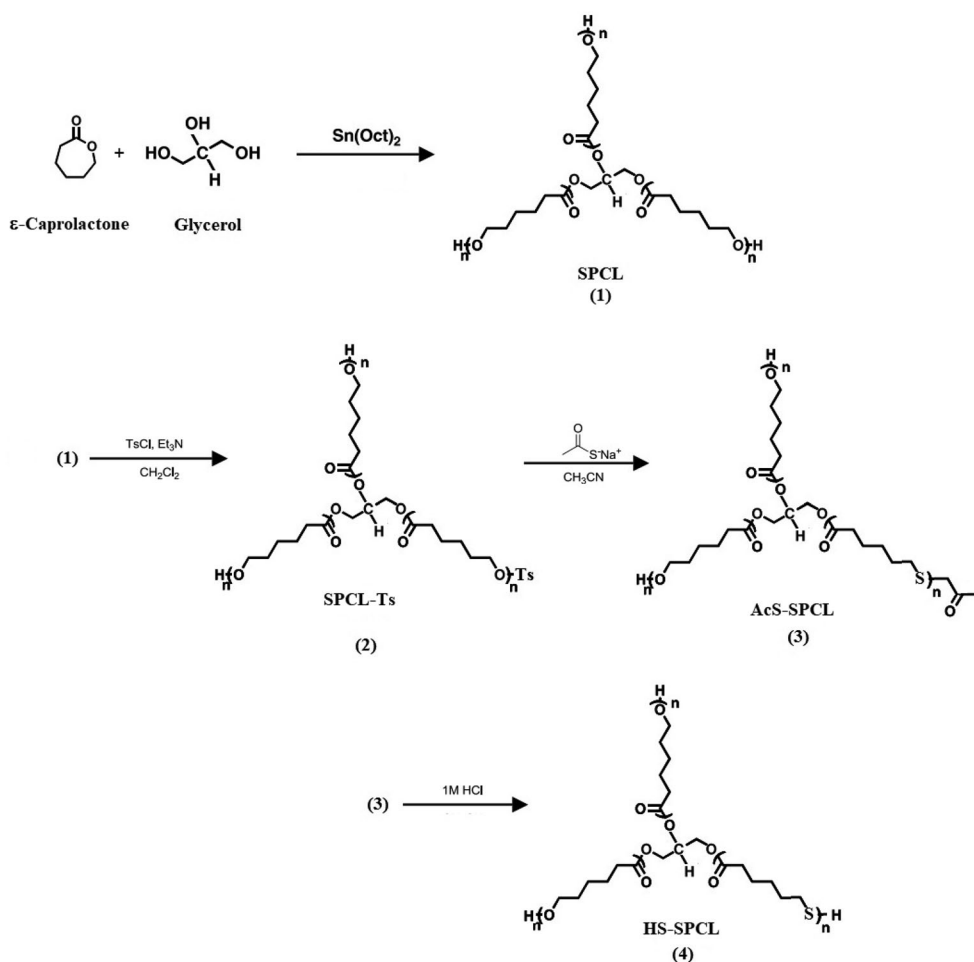


The precipitate was aged for 24 h at room temperature (25 °C). The precipitated HAPN was centrifuged and then washed with deionized water. The processes of centrifuging and washing were carried out three times. The resulting powder was dried in a freeze-drier system for 10 h followed by calcination at 900 °C for 1 h at the rate of 5 °C min⁻¹ in air. The resulting HAPN powder was analyzed by X-ray diffraction (XRD) and TEM.

2.4.1. Covalently coupling of mercapto-SPCL to HAPN

The hydroxyl groups of HAPN were activated after reaction with GPTMS. The epoxidized silane group was covalently bound to one or more hydroxyl groups on the surface of HAPN forming ether bonds and then allowing the epoxy group to react with the SH group of mercapto-SPCL(4). This method is an adaptation of the silanization technique commonly used to modify HAP and silica to covalently bind organic molecules to their surfaces [37].

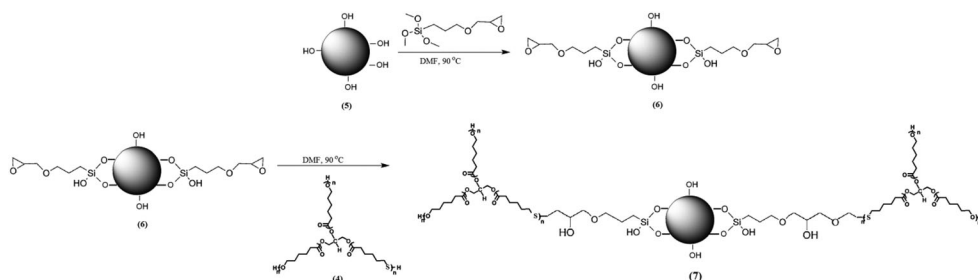
In the first step, 1.0 g of HAPN (5) were mixed with 50 mL of DMF in a two-neck-flask with a flow of N₂ and a Dean-Stark Trap. The solution was kept at 175 °C for 4 h and the distillate, approximately 10 mL, was removed. The solution was cooled to 95 °C and



Scheme 1. Illustration of the general approach used to synthesize the mercapto-SPCL (4).

the trap was changed into a condenser. A volume of 1.0 mL of GPTMS was added and the solution was kept at 95°C and left to react for 48 h. Then, a solution of SPCL(SH) (4) in DMF (1 g:50 mL) was dropped into the flask containing the functionalized HAPN powder (6) and left to react for 72 h at 95°C . After this, the mixture was filtered and subsequently washed two times with DMF and two times with deionized water. Finally, the powder containing SPCL-g-HAPN was washed using Soxhlet extraction with DCM at reflux temperature for 2 days to the removal of SPCL homopolymer formed during the grafting reaction and after was washed with EtOH in excess. The white powder was obtained and it was dried overnight under a vacuum at 60°C . The complete scheme for the synthesis of the hybrid SPCL-g-HAPN (7) is illustrated in [Scheme 2](#).

The weight-loss of HAPN and SPCL-g-HAPN samples was investigated by employing thermogravimetric analysis (TGA Mettler-Toledo TGA/STDA 851). The samples were heated to 700°C at a heating rate of 5°C min^{-1} under an Ar atmosphere (10 mL min^{-1}) to estimate the content of SPCL on the HAPN particles. The percent of grafting yield ($\% G_y$) and percent graft efficiency ($\% G_e$) was calculated by:



Scheme 2. Illustration of the synthetic route for SPCL grafting onto HAPN.

$$\%G_y = W_{G,HAPN} - W_{R,TGA} \quad (2)$$

$$\%G_e = \frac{W_{HAPN} - W_{HS-SPCL}}{W_{HS-SPCL}} \quad (3)$$

where $W_{G,HAPN}$, $W_{R,TGA}$, W_{HAPN} and $W_{HS-SPCL}$ are the weights of grafted HAPN, the residue of TGA, HAPN, and mercapto-SPCL, respectively.

Zeta-potential measurements (ZP) were performed by a Zeta-sizer (Nano-ZS) from Malvern Instruments and a Dispersion Technology Software (DTS). The Zetamaster 5002 took an average of five measurements at the stationary level. The cell used a 5 nm × 2 nm rectangular quartz capillary. The ZP were made at room temperature (25 °C). All measurements were carried out using HAPN and SPCL-g-HAPN at concentrations of 2.90 μg mL⁻¹. For the ZP measurements, the samples were suspended by vortex in PBS for 10 s.

2.5. Biological assays

2.5.1. Protein adsorption studies

HSA and HFb were iodinated with labeled NaI¹²⁵ by using the modified chloramine T method [38]. From 0.25 to 1.00 g of protein was dissolved in 0.375 mL of PBS. Then, 1.0 mCi NaI¹²⁵ was added (specific activity 17.4 Ci mg⁻¹ and concentration 100 mCi mL⁻¹) to the reaction mixture. The solution was capped and allowed to stand unagitated for 30–35 min. The reaction was stopped by passing the reactants through two previously characterized Sephadex G-25 columns. The labeled protein was eluted entirely in the void volume while the remaining reactants and unwanted by-products were eluted in the last portion of the total volume. After the labeling procedures, the ¹²⁵I-HSA and ¹²⁵I-HFb solutions were chromatographically purified in a column packed with Sephadex G-100 against PBS solution to remove any unbound ¹²⁵I radioactive label. The percentage of labels bound to the HSA and HFb determined by chromatographic methods [39] was more than 98.0%. The final activities of the ¹²⁵I-HSA and ¹²⁵I-HFb were 1.68.10⁸ and 3.8.10⁶ cpm mg⁻¹, respectively.

All radiolabeled proteins were freshly prepared and were discarded after 24 h. All iodination's had a degree of labeling of approximately 1.0 labels per protein molecule. To ensure that the iodination procedure did not denature the proteins, all

radioiodinated proteins were characterized by ultraviolet spectroscopy (UV) and fluorescence spectroscopy (FS) to check their integrity after the radiolabelling process.

Protein adsorption onto HAPN and SPCL-g-HAPN substrates were done in 5 mL adsorption cells according to previous works [40, 41]. About 300 mg of the substrates were introduced into the cells. The closed cells were then primed with degassed PBS at room temperature (25 °C) until all air was removed. The cells were allowed to sit at room temperature (25 °C) for at least 1 h before the introduction of the labeled protein solution. Radiolabeled protein solutions were then injected into the cell to remove all priming buffer and to introduce the ^{125}I -HSA or ^{125}I -HFb protein solution in desired concentrations [41]. Care was taken so as not to introduce any air into the system. The cells were then allowed to remain stationary, at room temperature (25 °C), for up to 24 h. To terminate protein adsorption each cell was flushed with 20 mL PBS to ensure that the substrates were not removed through a protein-solution at air interface. Contact of the solid HAPN and SPCL-g-HAPN surfaces with the liquid-air interface was avoided during the adsorption experiments and the rinsing procedures. This is important because 'denatured' protein layers might be deposited on the HAPN and SPCL-g-HAPN. Adsorbed protein concentrations were determined by gamma counting on a gamma radiation detector (Packard Cobra-II gamma counter). The background was estimated from tubes exposed to tracer ^{125}I -HSA or ^{125}I -HFb but lacking powders. Three replicates were used and the counts from each sample were averaged and the protein surface concentration was calculated according to Equation (4):

$$\text{Protein (mg g}^{-1}\text{)} = \frac{[\text{Counts (cpm)} \times C_{\text{solution}}(\text{mg mL}^{-1})]}{[\text{SA}_{\text{solution}}(\text{cpm mL}^{-1}) \text{ m (g)}]} \quad (4)$$

where the counts are the radioactivity measurements from the HAPN and SPCL-g-HAPN, and the C_{solution} and $\text{SA}_{\text{solution}}$ are the concentration and the specific activity of the protein solution, respectively.

After the adsorption of ^{125}I -HSA or ^{125}I -HFb, samples were exposed to not radio-labeled HSA and HFb proteins, respectively. After each step, the radioactivity was measured to study the elutability. In the case of ^{125}I -HSA or ^{125}I -HFb molecules weakly adsorbed to the surface, these would be replaced by unlabeled proteins.

After normalization of the results for mass (m) the amount of adsorbed protein (Γ) at each solution concentration (C) was calculated and fit to the Langmuir equation (Equation 5) [41]:

$$\Gamma = \frac{\Gamma_{\text{max}}kC}{(1 + kC)} \quad \text{or} \quad \frac{C}{\Gamma} = \frac{C}{\Gamma_{\text{max}}} + \frac{1}{k \cdot \Gamma_{\text{max}}} \quad (5)$$

where Γ_{max} is the monolayer adsorption capacity and k is the Langmuir constant or association constant, which is a measure of the apparent affinity of the protein with the surface. All the data points were repeated with three replicates.

2.5.2. MG-63 cell attachment and proliferation

MG-63 cells were used to assay the osteoblastic cell response on the SPCL-g-HAPN surfaces. Samples discs of HAPN, SPCL, and SPCL-g-HAPN of 10 mm in diameter and 1 mm thickness were sterilized at room temperature (25 °C) by gamma rays at 25

kGy, placed into 24-well cell culture dishes, and seeded with MG-63 cells in a density of 2.0×10^4 cells well⁻¹. The cells were cultured in DMEM containing 10% FBS, 1% PCN-STM. The cells were cultured for 3 and 5 days at 37 °C in a humidified air atmosphere containing 5% CO₂. Three samples were used for each experimental group and time interval. Following the incubation period with HAPN, SPCL, and SPCL-g-HAPN the MG-63 cells were washed with PBS. Cells were fixed for 5 min in a 3.7% FD solution in PBS. After washing extensively with PBS, samples were dehydrated with ACE and the adhered cells were permeabilized with 0.1% Triton® X-100 and thoroughly washed again with PBS. Cells were stained with a 50 µg mL⁻¹ FITC-PHN conjugate solution in PBS (containing 1% DMSO from the original stock solution) for 40 min at room temperature (25 °C) to stain the DNA of the MG-63 cells. After washing with PBS solution to remove unbound FITC-PHN, samples were incubated for 10 min at room temperature (25 °C) with 1 µL of AO/EtBr (1:1) staining solution to detect apoptosis. Samples were mounted in vector shield fluorescent mounting (Vector Laboratories, UK) and observed in a Leica TCS SP5 laser scanning confocal microscope. The culture media in DMEM was used as a negative control group.

2.5.3. Cytotoxicity assay

The cytotoxicity of materials was evaluated *in vitro* using the indirect contact assay, based on the ISO (International Organization of Standardization) standards [42]. The cells were kept in contact with SPCL and SPCL-g-HAPN extracts for 24 and 72 h. The SPCL and SPCL-g-HAPN extracts were produced with the incubation of the samples in a complete culture medium at 37 °C in a proportion of 0.1 g mL⁻¹ for 24 h. After that, the solution was diluted in a proportion of 1:1 and 1:3 with a complete medium. The MTT reduction method was used to measure cell viability in this case, since only live cells can metabolize this salt, which measures the mitochondrial activity. Cells were incubated for 4 h in MTT reagent solution (0.5 mg mL⁻¹) diluted in culture medium. The optical density (OD) was measured with a plate reader (Agilent Bio Tek) at 590 nm.

2.5.4. Susceptibility of SPCL-g-HAPN to enzymatic degradation

The susceptibility of SPCL-g-HAPN to LIPH and CHE hydrolysis were studied by turbidimetry according to the modified procedure reported by literature [43]. Initially, emulsions were prepared by suspending 0.5 g of the SPCL-g-HAPN in 50 mL of CHCl₃. By using an ultrasonic disruptor the initial solution was poured into 250 mL of 0.02 M PBS containing 0.01 wt% of the surfactant Plysurf A210G to attain a hydrophile/lipophile balance (HLB) of 9.6. The obtained emulsion was submitted to the sonication for 30 min for stabilization of the formed emulsion. The emulsion was submitted to a rotary evaporator system (Laborglas, LGI-RE-100) at 40 °C to remove the CHCl₃ resulting in an emulsion with a polymer concentration of 1 mg mL⁻¹.

Stock enzyme solutions of LIPH (1800 U) and CHE (1600 U) in 2 mL each of 0.02 M PBS (pH = 7.4) were prepared. Each stock solution was added to 98 mL of SPCL-g-HAPN emulsion to form 100 mL of enzyme-containing emulsion with an enzyme/polymer ratio of 0.3 for LIPH and 0.5 for CHE. The emulsions were

continuously agitated at 37 °C and the OD were measured with a UV-Vis spectrophotometer (Varian, Cary 50) at 650 nm against distilled water. Control emulsions were monitored for any evidence of optical turbidity reduction in the absence of enzymes.

2.5.5. Alkaline phosphatase activity

SPCL-g-HAPN discs (0.8 cm²) were fixed to the bottom of the tissue culture plates (48 well) with inert vacuum grease. MG-63 cells at a set density of around 2.0×10^4 cells cm⁻² were placed on specimens or the well bottom in DMEM supplemented with 5% FBS, and the medium was changed every 24 h during incubation in a CO₂ incubator. The alkaline phosphatase (ALP) activity on each specimen was determined after 1, 3, 5, and 7 days. To remove the unattached cells, specimens were gently washed with PBS solution. Each specimen was incubated with 100 μL of o-NPP solution at 37 °C for 30 min. The production of o-nitrophenol in the presence of ALP was measured by monitoring light absorbance by the solution at 405 nm using an ELISA reader. The ALP activity was calculated as nanomols of reaction product (o-nitrophenol) per minute from a mass of cellular protein.

2.6. Statistical analyses

The results were expressed as the mean ± standard deviation obtained from 3 samples for each experimental group. All data were subjected to statistical analysis using either Student's t-test or one-way analysis of variance (ANOVA). Differences were considered statistically significant at $p < 0.05$.

3. Results and discussion

3.1. SPCL synthesis and characterization

To allow the O/I hybrid based on covalently coupling of SPCL onto HAPN thiol groups were attached to SPCL chains. Initially, SPCL was synthesized by reacting glycerol with an ε-caprolactone monomer by using glycerol as core and Sn(Oct)₂ as initiator. Sn(Oct)₂ is a catalyst widely used for the ring-opening polymerization (ROP) of lactones and lactides due to its high activity as well as its approval by the American Food and Drug Administration (FDA-EUA) for the synthesis of polymers used in food coatings [44]. Glycerol is a bio-based renewable feedstock, which could be used as a source for producing biodegradable polyesters for the biomedical field [45].

In this work, glycerol was used as an initiation center for performing polycondensation reactions in the presence of the cyclic ε-CL monomer yielding SPCL. The synthesis of the SPCL appears to involve the coordination of the Sn(Oct)₂ and the glycerol with the cyclic ester ε-CL monomer forming an initiating tin-complex followed by ROP [46]. In this mechanism, the Sn(Oct)₂ is the catalyst while the glycerol is an initiator. The Sn(Oct)₂ and the glycerol react together resulting in the formation of tin(II) alkoxides which then become the 'true' initiators to form SPCL. For confirmation of the SPCL structure, the ¹H-NMR and ¹³C-NMR spectra were measured and are shown in Figure 1. The resonance peaks (a–e) are attributed to the

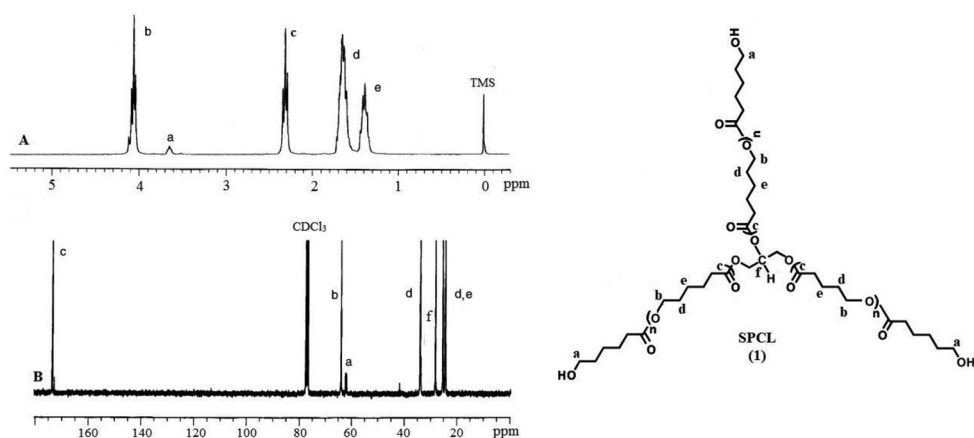


Figure 1. ¹H (A) and ¹³C (B) NMR spectra of SPCL. The spectra were obtained in CDCl₃ at room temperature (25 °C). TMS: tetramethylsilane.

polymer backbone of the SPCL arms (Figure 1(A)). A weak signal at δ 3.6 ppm indicates the presence of a hydroxyl group at the end of the SPCL arm. The very low resonance signal of this peak (Figure 1(A)) suggests the presence of intra-molecular hydrogen bonding. The ¹³C-NMR spectrum of SPCL is shown in Figure 1(B). No carbon peaks adjacent to the glycerol hydroxyls were observed in ¹³C-NMR spectrum (Figure 1(B)) suggesting that hydroxyls of glycerol were completely converted into the PCL arms. A typical ¹³C-NMR spectrum of SPCL is shown in Figure 1(B). It indicates a chemical shift δ at 173.5 ppm corresponding to the carbonyl group in the SPCL arm. High-intensity signals at 64.0 ppm in the spectrum corresponded to carbon (b) atom in the unit located in the middle of the SPCL arms, whereas a small peak at 62.6 ppm is indicative of the carbon atom (a) in the unit located at the end of the SPCL arms (Figure 1(B)). All these results from the ¹H-NMR and ¹³C-NMR spectra confirm that three-arm SPCL at 92% yield has been successfully synthesized.

The molecular weight of the synthesized SPCL was characterized by Maldi-Tof spectroscopy (Figure 2(A)). The peak-to-peak distance in the spectrum reveals the molecular mass of the repeating unit characterized by a mass increment of 114 Da and can be assigned to the mass of the repeating ϵ -CL unit terminated with a hydroxyl group (Figure 2(A)). The average molecular weights determined using Maldi-Tof MS were in the 4.526–7.262 kDa range (Figure 2(A)) and molecular weight subdistributions could not be detected suggesting that the characteristic structure of a star polymer with the overall structure of SPCL was synthesized.

The GPC results of SPCL showed monodisperse curves and a single peak (Figure 2(B)), suggesting a single ring opening polymerization (ROP) mechanism without the presence of secondary reactions that can generate homopolymers of ϵ -CL at least not to any significant extent. The molecular weights of a three arms SPCL ranged from 5430 (M_n) to 8280 (M_w) with an M_w/M_n ratio of 1.53 which is in reasonable concordance with Maldi-Tof measurements. The values of the molecular weight determined by GPC are slightly higher than the calculated

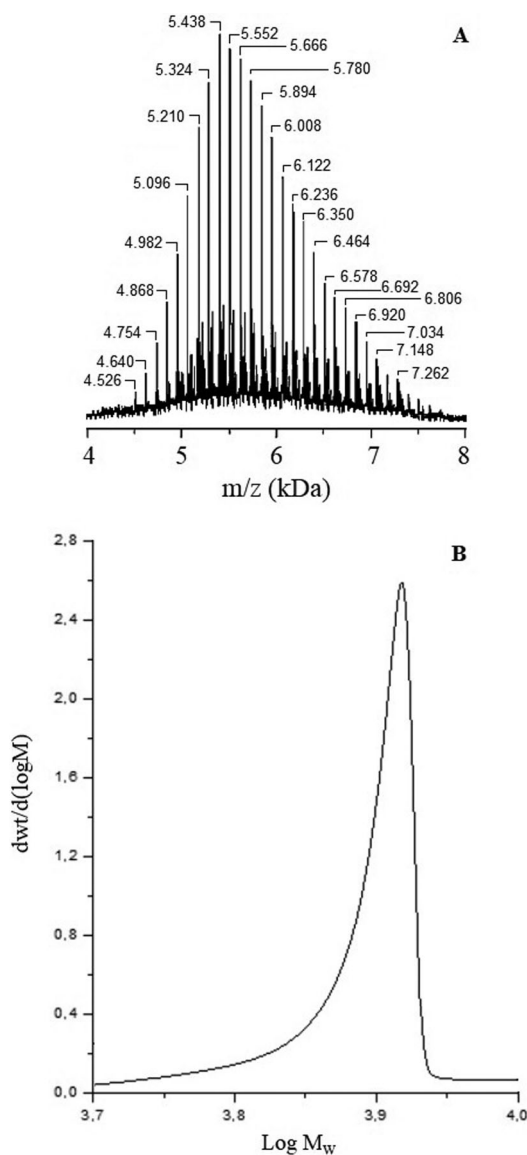


Figure 2. Maldi-ToF spectra (A) and GPC curve (B) of SPCL.

molecular weights from Maldi-ToF probably due to the smaller hydrodynamic volume of SPCL and the calibration of the GPC system being performed with linear polystyrene standards. Maldi-ToF and GPC results indicated that the SPCL was prepared successfully.

3.2. Synthesis and characterization of the hybrid SPCL-g-HAPN

The thiol groups were introduced in SPCL using a modified thioacetate method which is accomplished by conversion of tosylate to the thiol through thioacetate-

protected SPCL. This is easily hydrolyzed by 1.0 M HCl to form the final product (Scheme 1). Since three arms of SPCL has three terminal OH groups, tosylation occurs on both ends, but adding 1 mol equivalents of p-toluenesulfonyl chloride to SPCL produced a 65% yield of monotosylate (2) and 15% yield of ditosylate (3), in good agreement with other methods reported by literature to synthesize mercapto-dendritic-polymers [47, 48].

To check the SPCL grafting, the dispersibility of SPCL-g-HAPN in DCM was compared with the untreated HAPN and the results are shown in Figure 3. The dispersibility of the SPCL-g-HAPN was characterized by the time dependence of the weight of nanoparticles suspended in DCM. The SPCL-g-HAPN (0.1 g) and the solvent (40 mL) were introduced into a glass vessel and the suspension was stirred with the aid of ultrasonic oscillation until an excellent dispersion of the particles in the solvent was attained. A portion of liquid (5 mL) was taken out of the suspension at different time intervals and the optical density (OD) at 600 nm was measured. The amount of the suspending particles in the solution was determined by the difference between the OD of this liquid and the OD of the pure solvent having the same volume. The results shown in Figure 3 indicate a remarkable improvement in dispersibility resultant from SPCL surface grafting onto HAPN. Ungrafted HAPN completely precipitates after a few hours. On the contrary, SPCL-g-HAPN gives a stable colloidal dispersion in the solvent indicating that grafted HAPN tends to be more stable and suggests that the grafting of SPCL onto HAPN influences the agglomeration states of the composite nanoparticles.

The XPS analysis of SPCL will confirm the chemical transformation of the HAPN surfaces. In general, the stronger the carbons signal (C_{1s}), more the SPCL has grafted on the surface of the HAPN nanoparticles. These transformations in the HAPN surface are outlined in the modification of the electronic structure of C_{1s} peaks

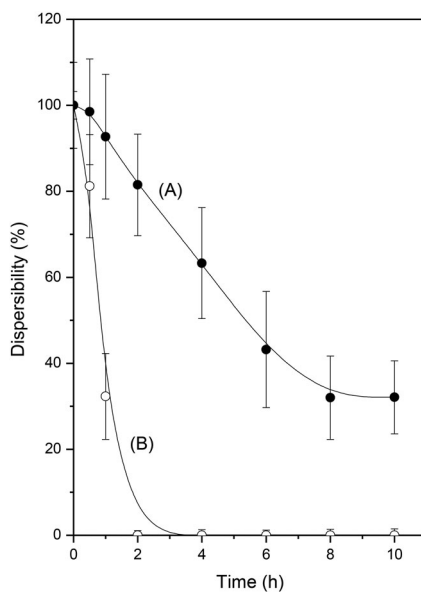


Figure 3. Dispersibility of SPCL-g-HAPN (A) and HAPN (B) in DCM at room temperature (25 °C).

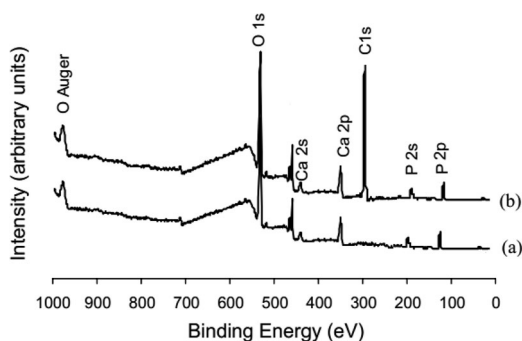


Figure 4. XPS spectra of HAPN control powder (a) and SPCL-g-HAPN (b).

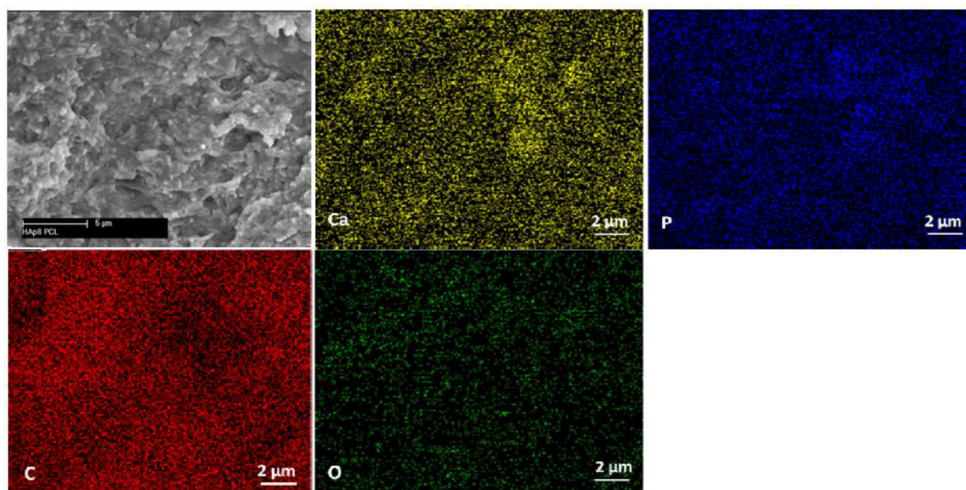


Figure 5. Scanning electron microscopy (SEM) micrograph and corresponding elemental mapping of the SPCL-g-HAPN showing Ca, P, C and O distribution. The first micrograph at the top (left) corresponds to the SEM area examined.

concerning the untreated HAPN surfaces. **Figure 4** shows the XPS spectra of SPCL-g-HAPN. The C_{1s} and O_{1s} peaks increase significantly with the SPCL grafting of HAPN. This strongly suggests the presence of SPCL on the HAPN surface. Elemental XPS mapping analysis (**Figure 5**) showed that a relatively homogeneous distribution of Ca, O, P and C elements are present in SPCL-g-HAPN indicating the homogeneity of the SPCL grafting and further confirming that SPCL-g-HAPN was successfully synthesized.

Figure 6 shows the XRD patterns for HAPN and SPCL-g-HAPN samples. As can be seen in all cases, two strong diffraction peaks at Bragg angles $2\theta = 21.4^\circ$ and 23.8° could be observed, which was attributed to the diffraction of the (1 1 0) lattice plane and the (2 0 0) lattice plane of semi-crystalline SPCL, respectively [49]. The grafting of SPCL should be an event occurring only at the HAPN surface. Once the state of the bulk properties such as crystallinity and the crystalline phase has been changed by the chemical reaction, the functionalized HAPN may change its intrinsic

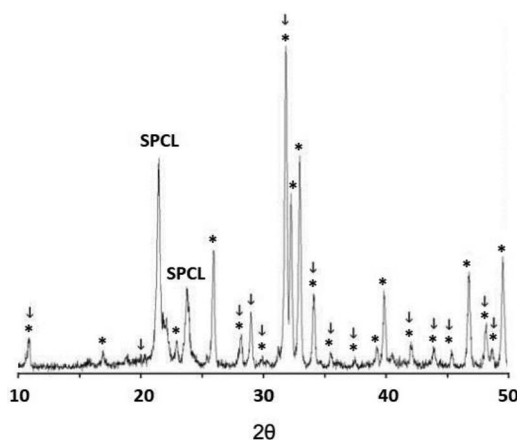


Figure 6. X ray diffractogram of the SPCL-g-HAPN composite: (*) indicates the HAPN phase and (↓) suggests the β -TCP phase compared to International Center for Diffraction Data (ICDD) 74-0566 and 9-0169 standards, respectively.

properties. The XRD patterns in [Figure 6](#) indicate that both the ungrafted HAPN and SPCL have the characteristic peak at 2θ regions of 26° , 29° , 32° – 34° , 40° , 46° – 49° , which are consistent with the HAPN phase (ICDD 09-432). XRD patterns of HAPN and SPCL-g-HAPN present very broad peaks suggesting the presence of nanosized crystals [50]. Our results suggested that the selected SPCL chains are on the HAPN surface and the intrinsic properties of HAPN, especially the crystalline structure, were unaltered.

3.3. Thermal analysis

The grafting of SPCL surrounding HAPN could affect the interface between the polymer phase and the ceramic nanoparticles. Since the mechanical properties of polymer composites could be critically affected by the interface, the quantitative analysis of the grafted SPCL should be investigated. The amount of surface-grafted SPCL was determined by the TGA method. [Figure 7](#) represents the TGA curves of HAPN, SPCL-g-HAPN, and SPCL, respectively. The HAPN, SPCL-g-HAPN, and SPCL displayed 4.5 wt%, 24.78 wt%, and 100 wt% in weight loss at 600°C , respectively. The weight loss for HAPN of 4.5 wt% corresponds to the removal of adsorbed water [51]. SPCL-g-HAPN shows appreciable weight loss at 600°C ([Figure 7](#)). The total mass loss at 600°C by SPCL-g-HAPN samples leaves a 75.22% residual weight, which is attributed to the decomposition of the grafted SPCL chains. The difference in the mass loss between the bare HAPN and the SPCL-g-HAPN gives the grafted SPCL amount (or grafting yield) of 24.78%. The grafting efficiency (grafted SPCL as a percentage of total mercapto-SPCL used in the reaction) suggests a grafting efficiency of 61.7%. From the TGA curve of the SPCL ([Figure 7](#)) two steps in the decomposition are observed. SPCL showed high thermal stability based on the first step where the initial major thermal degradation temperature began at the range between 250 and 380°C with a weight loss of 76.9%. The second transition of the weight loss (23.1%) occurring at 380 – 440°C is due to the cleavage of the backbone of the SPCL that occurs above 440°C with the complete decomposition of the polymer chains.

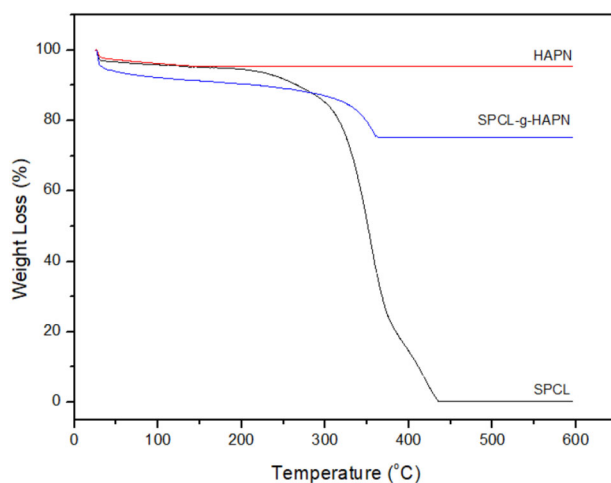


Figure 7. Thermogravimetric analysis (TGA) curves of HAPN, SPCL-g-HAPN and SPCL.

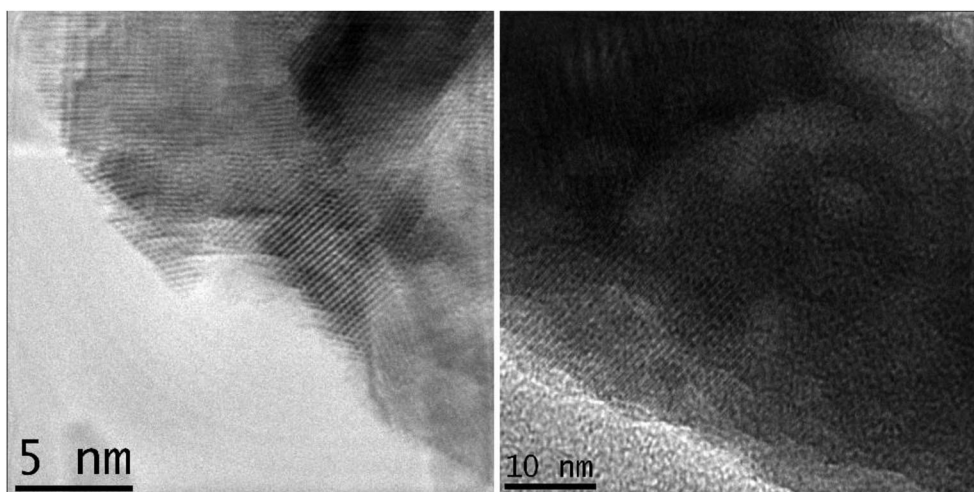
3.4. TEM analysis

Transmission electron microscopy (TEM) was carried out with HAPN and SPCL-g-HAPN and is presented in [Figure 8](#). Primary uncoated HAPN showed ellipsoidal nanoparticles with an average size of 9 nm ([Figure 8\(A\)](#)). The HAPN particles were well-ordered structures with d-spacing of 0.2886 and 0.3502 nm in the crystalline phase, corresponding to the (2 1 1) and (0 0 2) planes of the HAPN structure. Additionally, TEM images showed that HAPN were embedded in the SPCL grafted chains ([Figure 8\(B\)](#)) and suggests that the SPCL grafting reaction first creates nucleation sites at the HAPN surface. As the graft reaction increased and the condensation reaction between HAPN and SPCL continued, the nucleation sites grow together to form a continuous coating.

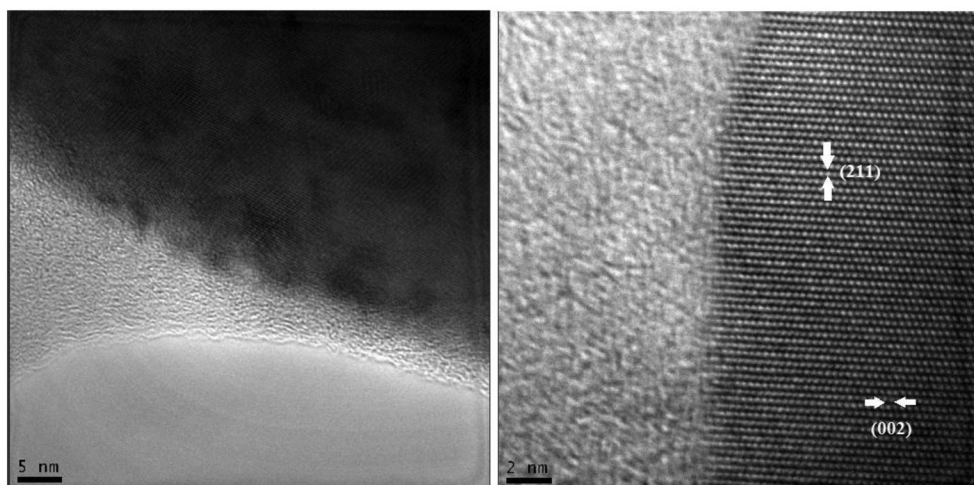
3.5. Zeta potential

Zeta potential measurement was used to determine whether the SPCL grafting can generate different surface-charged HAPN nanoparticles. The zeta potential of the SPCL-g-HAPN suspensions measured by the zeta potential analyzer is shown in [Figure 9](#). It can be observed that the SPCL-g-HAPN modified with SPCL has a zeta potential of -28.1 ± 3.2 mV while the ungrafted HAPN has a zeta potential of -11.7 ± 2.7 mV in PBS solution at pH 7.4 and 25 °C. The ZP values may be dependent on HAPN phase composition and particle size. The zeta potential values ([Figure 9](#)) indicated that HAPN corresponds to two phases of powders, HAPN and tri-calcium phosphate (TCP). For two-phase powder, the zeta potential reaches a value of -25 mV, while for HAPN and TCP powders this value is -20 and -5 mV, respectively, and are consistent with previous studies reported by literature [51].

It is well known that the ZP of HAPN is dependent upon particle size [52]. A slightly extended positive charge of the calcium ions from the surface of the SPCL would increase the distance between the slip planes resulting in a lower negative zeta potential of the HAPN nanoparticles. Therefore, large particles of SPCL-g-HAPN



(A)



(B)

Figure 8. Transmission electron micrographs of HAPN (A) and SPCL-g-HAPN (B).

may exhibit less negative zeta potential. As shown in TEM images (Figure 8), the length of some HAPN is larger than 8 nm, which is probably the reason for the lower values of zeta potential observed for the HAPN nanoparticles.

3.6. Biological assays

3.6.1. Protein adsorption

HAP coatings are generally considered to improve the osseointegration of biomedical implants. It is generally assumed that selective adsorption of plasma proteins to the implant surface material is a critical factor for cellular activation pathways. Several of these proteins are present in blood plasma such as albumin (HSA), von Willebrand

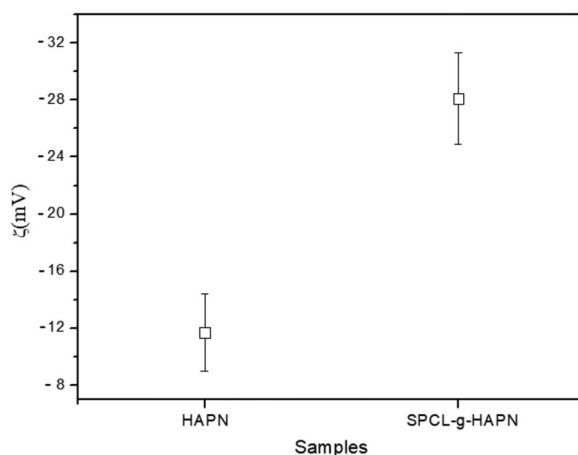


Figure 9. Zeta potentials measurements ($N=3$) of the HAPN and SPCL-g-HAPN in PBS solution at pH 7.4 and 25 °C.

factor, fibrinogen (HFb), and fibronectin. Even after a very short exposure time, these proteins bind to the synthetic surfaces that will influence further interactions with integrins and cellular activation pathways. It has previously been shown that a model system of fibrinogen and the major platelet membrane receptor (GPIIb-IIIa) can be used to predict the performance of the hemocompatibility of biomaterials [53]. The study of HSA and HFb adsorptions onto SPCL-g-HAPN will contribute to elucidating the mechanisms involved in the biocompatibility of the nanocomposite SPCL-g-HAPN.

It is well known that protein adsorption to synthetic surfaces depends essentially on the physical chemistry of surfaces such as surface tension, wettability, surface charge, and surface roughness [54]. Proteins generally have hydrophobic (neutral) and hydrophilic (neutral, negatively and positively charged) surfaces. Possible protein-surface interactions include electrostatic or ionic, both repulsive and attractive, van der Waals forces, hydrogen bonding, hydrophobic interaction, acid-base interactions and hydration forces. The ionic interactions, hydrophobic and van der Waals forces provide the most important adsorption driving force [55]. Additionally, different proteins can exhibit varying adsorption behavior on the same surface due to inherent characteristics specific to the protein. In this sense, HSA tends to have greater tendencies for the adsorption on hydrophobic surfaces and HFb shows an increased affinity for negatively charged surfaces [56].

To study the influence of SPCL grafting on protein interactions, the adsorption of ^{125}I -labeled HSA and HFb were quantitatively measured as a function of protein concentration. Isotherms resulting from adsorption of HSA and HFb are presented in Figures 10 and 11. In general, an initial slope indicating high protein affinity for the HAPN surface (Figure 10) characterizes the plots. The adsorption saturation yields a plateau value corresponding to the maximum amount of about $0.78 \mu\text{g g}^{-1}$ of HFb adsorbed by HAPN.

After the adsorption, HAPN and SPCL-g-HAPN powders were washed with protein-free PBS pH 7.4 for 10 min, the adsorbed HFb decreased and approached a

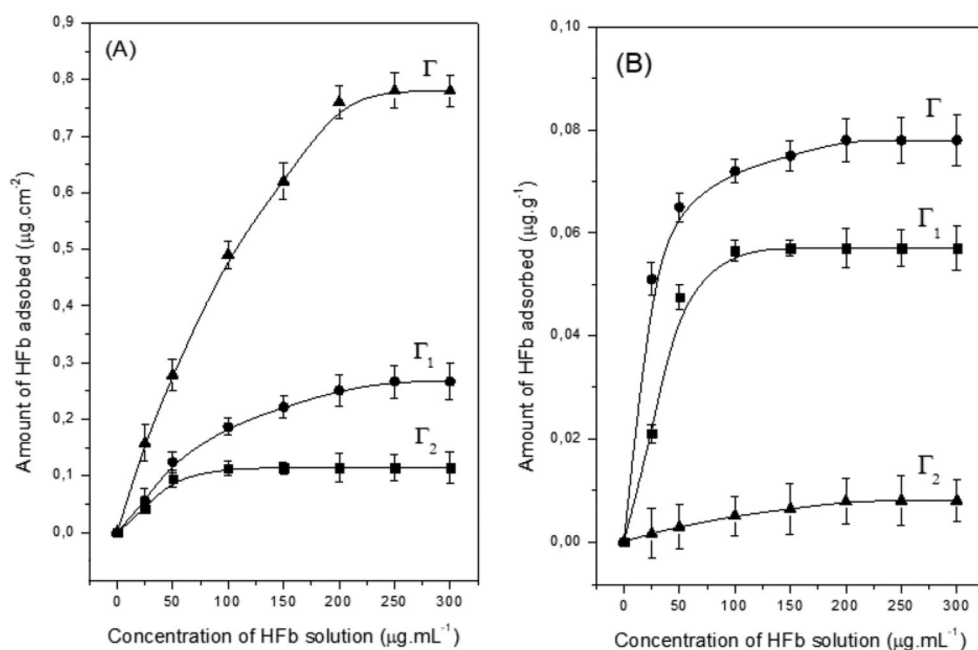


Figure 10. Isotherms for HFb adsorption onto HAPN (A) and SPCL-g-HAPN surfaces (B). Γ , Γ_1 and Γ_2 are the total adsorption amount, reversible adsorption amount and irreversible adsorption amount, respectively.

plateau that was lower than the previous adsorption isotherm and indicating the desorption of initially adsorbed HFb from HAPN and SPCL-g-HAPN surfaces, respectively. This result shows that part of the protein adsorbed is still adsorbed on the surface of HAPN powder after washing with PBS. In another word, only part of the protein was adsorbed in a reversible state concerning the dilution of the bulk phase. This part is referred to as reversible adsorption and is indicated by Γ_1 . The other part of the protein was adsorbed in an irreversible state concerning the dilution of the bulk phase, which is referred to as irreversible adsorption and indicated by Γ_2 . It can be seen in Figure 10(A) that for HAPN with increasing HFb concentration, both the Γ_1 and Γ_2 increase with descending slopes. The values of Γ_2 , increase with HFb concentration in low concentration regions and appear to a plateau after the concentration of $100\ \mu\text{g}\ \text{mL}^{-1}$. Hence, the fraction of irreversible adsorption by HAPN decreases with increasing total adsorption amount under the experimental conditions. Thus, HSA and HFb adsorption onto HAPN are irreversible over time. These results are consistent with observations of irreversible protein adsorption on HAPN nanocrystals [57].

The amount of adsorbed protein (Γ) at each solution concentration C was calculated and fit to the Langmuir according to Equation (5), and the correlation coefficients are $R^2 = 0.992$ and $R^2 = 0.999$ for HSA and HFb indicating the monolayer adsorption of proteins onto HAPN and SPCL-g-HAPN, respectively. It is observed (Figures 10 and 11) that at the lower concentration range, changes in the bulk concentration produced large changes in the amount of protein adsorbed, resulting in a

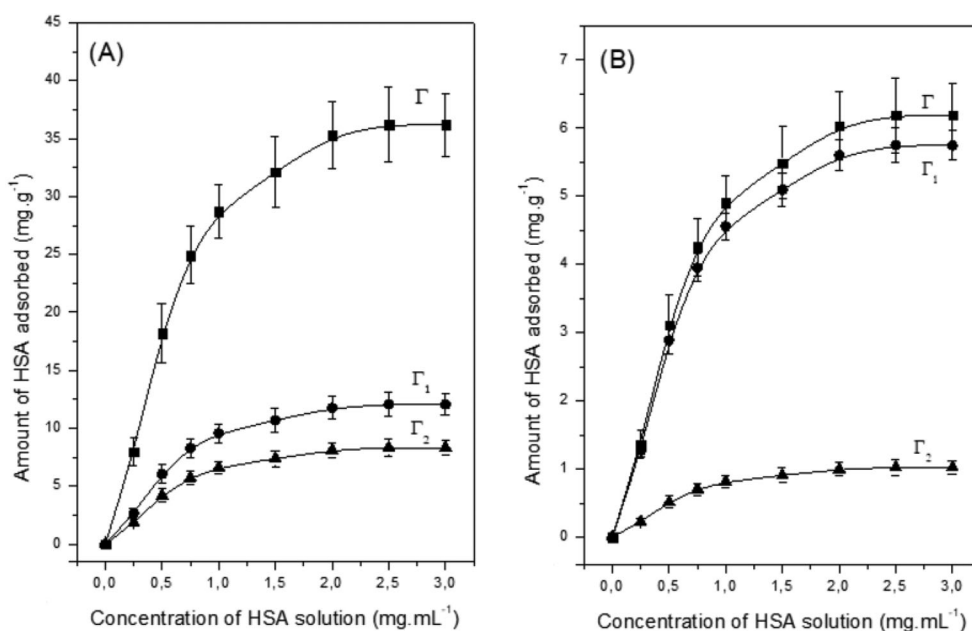


Figure 11. Adsorption isotherms for HSA on HAPN (A) and SPCL-g-HAPN surfaces (B). Γ , Γ_1 and Γ_2 are the total adsorption amount, reversible adsorption amount and irreversible adsorption amount, respectively.

Table 1. Monolayer adsorption capacity Γ_{\max} and association constant k obtained by fitting the isotherms in Figures 10 and 11 to the Langmuir equation ($R^2 = 0.999$ for HFb and $R^2 = 0.993$ for HSA).

Adsorption	Isotherm equation	Γ_{\max} (mg g ⁻¹)	k (mL mg ⁻¹)
HFb on nHAP	$C/\Gamma = 8.51C + 62.10$	1.2×10^{-3}	134.19
HFb on SPCL-g-nHAP	$C/\Gamma = 17.02C + 124.20$	0.59×10^{-3}	136.46
HSA on nHAP	$C/\Gamma = 0.022C + 0.014$	45.46	1.57
HSA on SPCL-g-nHAP	$C/\Gamma = 0.131C + 0.081$	7.63	1.62

roughly linear increase in adsorption. However, as the bulk concentration is increased, the adsorption is reduced and a plateau or a maximum adsorption level is reached. This type of adsorption behavior is characteristic of the Langmuir isotherm [58]. The corresponding monolayer adsorption capacity Γ_{\max} and the association constant k values from each isotherm are summarized in Table 1. Significant changes occurred in k (association constant) for SPCL-g-HAPN increased slightly ($k = 136.46$), indicating that SPCL-g-HAPN surfaces have a weaker apparent affinity by HFb at room temperature (25 °C) relatively to HAPN.

It has been noted widely in the literature that increased surface hydrophobicity promotes stronger protein adsorption from solution [59, 60]. Thus, it is expected that SPCL coating of HAPN surfaces decreases the wettability and the apparent affinity (k) of soluble protein with the surface increases [61, 62]. At 25 °C, the Γ_{\max} values for HFb on HAPN and SPCL-g-HAPN surfaces are 1.2 and 0.59 $\mu\text{g g}^{-1}$, respectively.

The interaction between the adsorbed protein molecules may be either attractive or repulsive, depending on the type and magnitude of the electric charge of the amino acid residues. These complicated processes involving protein adsorption are also reflected in the zeta-potential changes. The higher zeta-potential values of HAPN (Figure 9) confirmed that electrostatic forces were the primary mode of interaction with HSA or HFb. On the other hand, the decrease in zeta-potential confirmed the existence of hydrophobic interactions between HFb and HSA with SPCL-g-HAPN. The rise in surface charge on colloidal particles increased the magnitude of inter-particle electrostatic repulsion, which tended to disrupt existing protein aggregates and discourage further aggregation [63]. Consequently, the SPCL-g-HAPN could bind to HSA and HFb through a combination of electrostatic and hydrophobic interactions and could form micelle-like clusters.

3.6.2. Enzymatic degradation

Considering the bone tissue perspective, the SPCL-g-HAPN resembles the structure of bone tissue, where HAPN mimics the inorganic component and the SPCL component mimics the collagen-rich extracellular matrix. The SPCL-g-HAPN should combine biodegradability and bioactivity offering the opportunity to produce scaffolds with desired biological, physical and structural properties desirable for bone tissue engineering.

An important property of scaffolds when designing temporary or long-term implants for tissue engineering is their biodegradability. To partially mimic the *in vivo* biodegradation conditions, SPCL-g-HAPN samples were placed in a LIPH and CHE environment at physiological temperature (37 °C). The degree of SPCL-g-HAPN biodegradation was determined by the change in OD of the respective emulsions of the tested samples.

Figure 12 shows the change in the optical density (OD) of SPCL-g-HAPN emulsions as a function of time. It is observed that the enzyme degradation of SPCL-g-HAPN was significantly lower than the SPCL/HAPN blends. The initial slope of Figure 12 leads to the initial hydrolysis reaction rate ν_o that could be defined as $\left[\frac{d[\text{OD}]}{dt} \right]_{t \rightarrow 0}$ and $d[\text{SPCL}] \approx [\text{OD}]$. The OD reductions of the enzymatic reactions were intense enough to be optically monitored.

The ν_o values were 1.19 OD% h⁻¹ for SPCL/HAPN blends while for SPCL-g-HAPN ν_o values are 0.21 OD% h⁻¹. Significant differences in ν_o values were observed for the biodegradation between SPCL/HAPN blends and SPCL-g-HAPN nanoparticles. This result suggests that the grafting of SPCL on HAPN surfaces leads to the formation of a homogeneous hybrid O/I interface. In the SPCL-g-HAPN are potentially two types of degradable linkages, i.e. ester linkages at the SPCL chain and thioether linkages at the HAPN surface. Due to their different bond stabilities, the energy required for the hydrolysis of each bond would also be different.

It is well known that enzymes play an important role in catalyzing the hydrolysis of aliphatic polyesters such as PCL through hydrolytic scission of esters linkage of polymer backbone [64]. However, the mechanistic investigation of the enzyme biodegradability of SPCL-g-HAPN in this work is a complicated procedure. SPCL changes the properties of HAPN surfaces such as charge and hydrophobicity, as

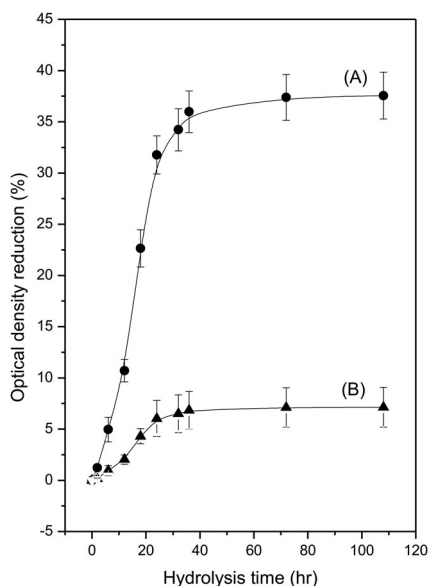


Figure 12. Enzymatic hydrolysis of SPCL/HAPN blends (A) and SPCL-g-HAPN (B). The composition of SPCL on SPCL/HAPN blends corresponds to the grafting of SPCL onto HAPN: 24.78%.

demonstrated previously by zeta potential (Figure 9) and contact angle measurements (Figure 14). Additionally, the enzymatic hydrolysis of SPCL-g-HAPN is a heterogeneous process that is affected by the mode of interaction between LIPH and CHE. Previous studies have shown that the catalytic activity of lipases is interfacially activated and the turnover of the enzyme may increase by orders of magnitude if the enzyme is presented to the substrate at an interface [65]. At the molecular level of the enzyme, the surface activation of LIPH also involves a conformational change within the enzyme, in which a surface domain, moves and exposes the active site region [66]. This open and active conformation of this type of LIPH is more hydrophobic than the closed state of the enzyme.

The SPCL-g-HAPN prepared in this study consists of an infiltration of the bioceramic HAPN with the polymer phase (SPCL) as schematically shown in Scheme 2. This approach is inspired by the fact that nearly 60 wt% of bone is constituted of an inorganic phase (hydroxyapatite) and the rest is the organic phase (collagen) and water [67].

The addition of the organic phase SPCL to HAPN is expected to enhance the dispersion of the inorganic phase on the SPCL chains. Thus, SPCL-g-HAPN should have more hydrophobic interfaces of SPCL chains compared to the ungrafted HAPN. More interfaces and more enzyme adsorption resulted in more SPCL scission and OD reduction of emulsions. In this sense, the SPCL-g-HAPN consists of SPCL as the surface hydrophobic domains and HAPN surface ungrafted sites as hydrophilic core domains.

3.6.3. MG-63 cell attachment and proliferation

Figure 13 shows the MG-63 cell proliferation after 1 and 4 days of culture on the SPCL-g-HAPN surface in comparison with cell culture dishes (CCD, negative

control). For control and all experimental groups, the results show an increase in cell proliferation with culture time. After 1 day of culture, the MG-63 cell proliferation on SPCL-g-HAPN surfaces was slightly different compared with ungrafted HAPN. After 4 days of culture, M-G63 cell proliferation appeared significantly superior for SPCL-g-HAPN compared with HAPN.

Studies have reported that cell attachment and adhesion to the culture substrate occur within minutes [68] and this cellular event is greatly affected by the characteristics of the material surface [69]. Thus, cell behavior at HAPN surfaces would be mostly affected after SPCL grafting as compared to those on ungrafted HAPN surfaces. It is well known that the wettability, i.e. the ratio of hydrophilicity to hydrophobicity of biomaterials surfaces, is considered a critical factor determining adhesion and cellular proliferation [70]. To assess the hydrophilicity of the SPCL-g-HAPN the static water contact angle was determined using static contact angle measurement.

As shown in Figure 14, the ungrafted HAPN sample exhibits a profoundly hydrophilic state exhibiting contact angles of $\theta = 12.8^\circ$. The SPCL grafting on the HAPN surface changes the contact angles to 76.8° leading to a wettability modulation of the bioceramics. It was believed that the improvement of modulation on hydrophilicity on SPCL-g-HAPN might be attributed to the modulation of hydrogen bonds between the numbers of OH groups of HAPN, respectively. Furthermore, the water contact value of SPCL-g-HAPN was closed to that of the cell culture dishes (CCD) (75.6°) (Figure 14). These results indicated that SPCL-g-HAPN would be more suitable for cell attachment than HAPN or SPCL alone because the optimum water contact angle of the surface for fibroblast adhesion is reported in the range between 55° and 75° [71].

3.6.4. Alkaline phosphatase activity

Along with the cell proliferation, the cell functionality was assessed by measuring the osteoblast differentiation markers such as ALP. The enzyme ALP exists in

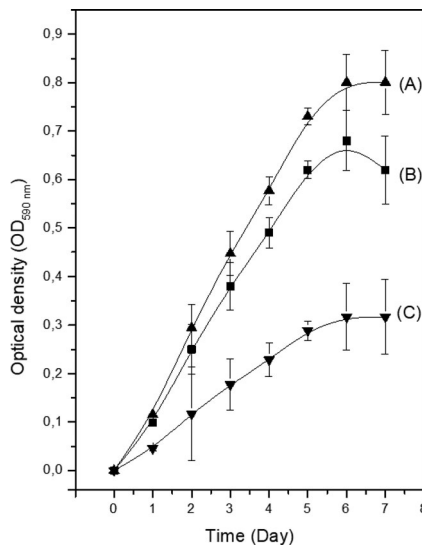


Figure 13. MG-63 cell proliferation levels on positive control (A), SPCL-g-HAPN (B) and HAPN (C) after culturing for up to 7 days. Negative control = cell culture plastic dish (CCD).

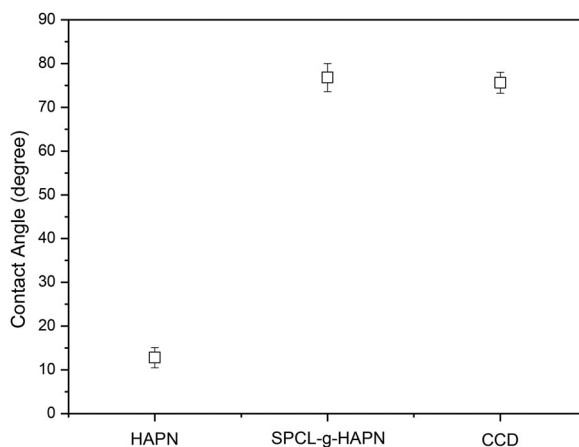


Figure 14. Static water contact angle of HAPN, SPCL-g-HAPN and CCD measured by sessile drop technique at room temperature (25 °C) ($N = 3$).

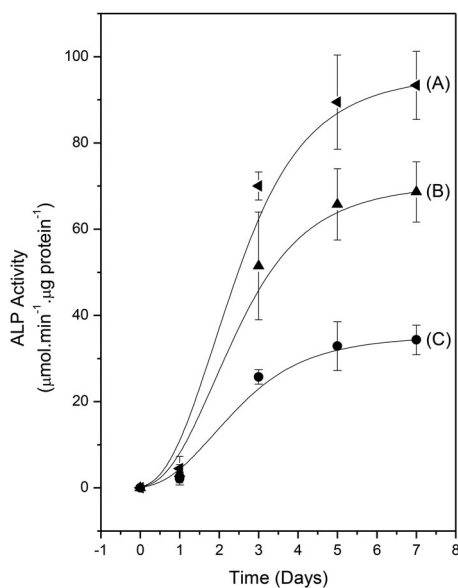


Figure 15. Alkaline phosphatase activity for osteoblastic phenotype expression of MG63 osteoblast-like cells cultured on SPCL-g-HAPN (B), HAPN (C) in comparison with cell culture plastic dish (negative control) (A).

intracellular membranes and its catalytic activity enhances the secretion of other extracellular matrix proteins, thus it is considered a marker for osteoblast differentiation at a relatively early stage [72].

To investigate the effect of the SPCL grafting onto HAPN surfaces on the cell differentiation behavior, the ALP activity was measured by culturing MG-63 cells on the SPCL-g-HAPN and HAPN surfaces in comparison with a cell culture plastic dish (positive control). Figure 15 shows that the ALP activity of control and all experimental groups increased with culture time. After 6 days of culture, ALP activities were slightly higher on SPCL-g-HAPN than on ungrafted HAPN. After 7 days, SPCL-g-

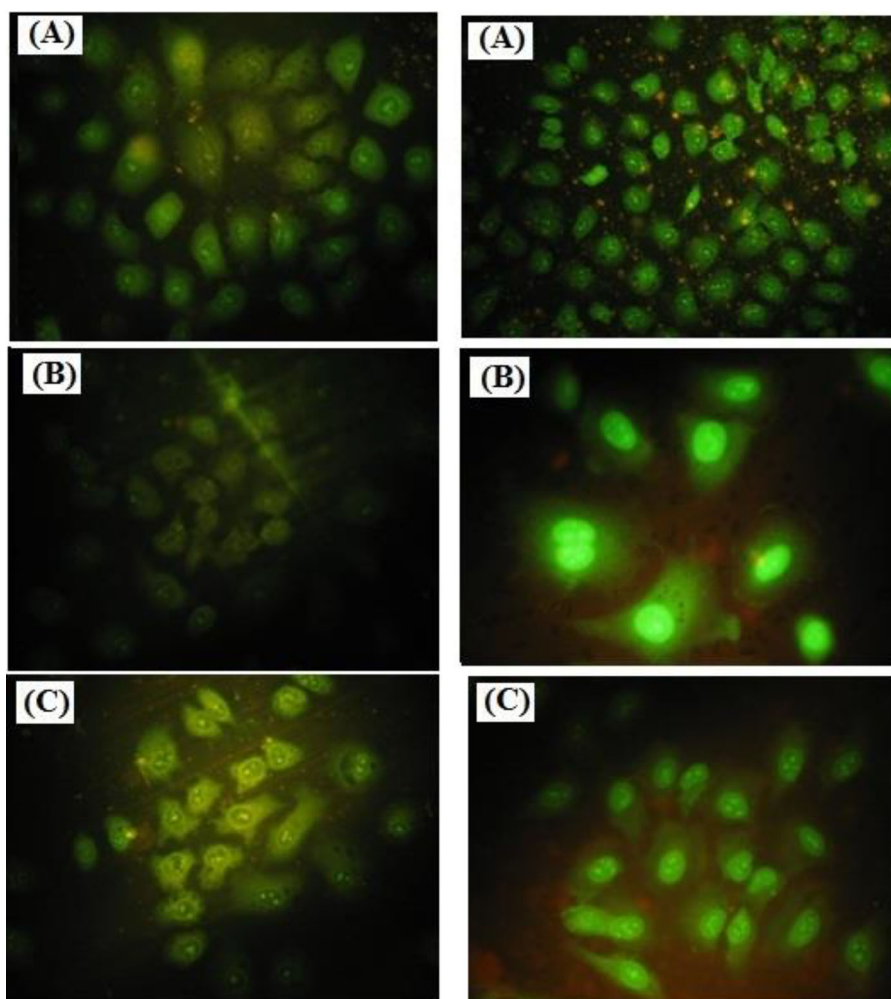


Figure 16. Representative epifluorescence micrographs after AO:EtBr staining of MG-63 cells seeded on CCD (negative control) (A), HAPN (B) and SPCL-g-HAPN (C) at 1 days culture. Magnification: 100 \times .

HAPN exhibited a significantly higher ALP level than the ungrafted HAPN surfaces. Based on these (Figure 15) it was confirmed that the grafting of SPCL onto HAPN provides significant adhesion and growth of the osteoblastic MG63 cells and induced them to differentiate at an enhanced level relative to the HAPN surface.

Even today, regenerative medicine prospects are still severely hampered by the host tissue response to the implantation of biomaterials. Despite the technological advances achieved regarding the new technologies of biomaterials that promise to recover the functionality of damaged organs and tissues, cellular and molecular events developed after implantation define the success of the biomaterial candidate and tissue regeneration. The use of SPCL-g-HAPN as a biomaterial requires the study of how it affects the biological tissue around to provide a suitable biomimetic environment to ensure cell survival, as well as target the desired cellular behaviors for the implant such as apoptosis [73]. Figure 16 illustrates an epifluorescence microscope

image of HAPN and SPCL-g-HAPN where MG63 cells grown for 1 day were stained with AO and EtBr. As is possible to observe, cells show a good level of adhesion to the SPCL-g-HAPN and changes associated with apoptosis were not observed in this work (Figure 16).

4. Conclusions

In this work, SPCL was successfully grafted onto HAPN to fabricate hydrophilic/hydrophobic domains at a bioceramic surface at appropriate conditions. This was supported by TEM, XPS, XRD, zeta potential and contact angle analysis. The hybrids SPCL-g-HAPN showed resistance to HFb adsorption. The degradation rates of SPCL-g-HAPN were slower than that of the corresponding SPCL/HAPN blends. The hydrophilicity evaluation and the measurements of chemical compositions of SPCL-g-HAPN surfaces suggested an SPCL enrichment process on the surface of HAPN prevented the contact of lipase and cholesterol esterase with SPCL chains and thus decreased the degradation rate.

The *in vitro* biological studies using human osteoblast-like cells (MG-63) showed that the cells had normal morphology and they were able to attach and spread out on SPCL-g-HAPN surfaces. It is expected that SPCL-g-HAPN to be useful to improve cell-seeding subsequent tissue growth in tissue-engineered products.

Disclosure statement

No potential conflict of interest was reported by the author(s).

Funding

The National Council for Scientific and Technological Development (CNPq) financially supported this study under grant 307609/2018-9.

ORCID

Alvaro Antonio Alencar de Queiroz  <http://orcid.org/0000-0002-1769-7022>

References

- [1] Frier B. Roman life expectancy: Ulpian's evidence. *Harv Studies Class Philol.* 1982;86: 213–251.
- [2] Ott HC, Matthiesen TS, Goh S, et al. Perfusion-decellularized matrix: using nature's platform to engineer a bioartificial heart. *Nat Med.* 2008;14(2):213–221.
- [3] Hiles M, Levitsky S. Interactive biomaterials: taking surgery to the next level. *Int Surg.* 2005;90:S13–S20.
- [4] Niemeyer CM. Nanoparticles, proteins, and nucleic acids: biotechnology meets materials science. *Angew Chem Int Ed.* 2001;40(22):4128–4158.
- [5] Tan J, Saltzman WM. Biomaterials with hierarchically defined micro- and nanoscale structure. *Biomaterials.* 2004;25(17):3593–3601.

- [6] Hench LL, Polak JM. Third-generation biomedical materials. *Science*. 2002;295(5557):1014–1017.
- [7] Biggs MJ, Richards RG, Gadegaard N, et al. Interactions with nanoscale topography: adhesion quantification and signal transduction in cells of osteogenic and multipotent lineage. *J Biomed Mater Res A*. 2008;18:399–404.
- [8] Lamers E, Walboomers FX, Domanski M, et al. The influence of nanoscale grooved substrates on osteoblast behavior and extracellular matrix deposition. *Biomaterials*. 2010;31(12):3307–3316.
- [9] Hutmacher DW. Scaffolds in tissue engineering bone and cartilage. *Biomaterials*. 2000;21(24):2529–2534.
- [10] Hench LL. Bioceramics, from concept to clinic. *J Am Ceram Soc*. 1991;74(7):1487–1510. [10.1111/j.1151-2916.1991.tb07132.x](https://doi.org/10.1111/j.1151-2916.1991.tb07132.x)
- [11] Kumar D, Gittings JP, Turner IG, et al. Polarization of hydroxyapatite: Influence on osteoblast cell proliferation. *Acta Biomater*. 2010;6(4):1549–1554.
- [12] Nakamura S, Kobayashi T, Yamashita K. Extended bioactivity in the proximity of hydroxyapatite ceramic surfaces induced by polarization charges. *J Biomed Mater Res*. 2002;61(4):593–599.
- [13] Kobayashi T, Nakamura S, Yamashita K. Enhanced osteobonding by negative surface charges of electrically polarized hydroxyapatite. *J Biomed Mater Res*. 2001;57(4):477–484.
- [14] Gittings JP, Bowen CR, Turner IG, et al. Polarization behavior of calcium phosphate based ceramics. *Mater Sci Forum*. 2008;587–588:91–95.
- [15] Orlovski VP, Zakharov NA, Ivanov AA. Structural transition and dielectric characteristics of high purity hydroxyapatite. *Inorg Mater*. 1996;32:654–656.
- [16] Kim HM, Rey C, Glimcher MJ. X-ray diffraction, electron microscopy, and Fourier transform infrared spectroscopy of apatite crystals isolated from chicken and bovine calcified cartilage. *Calcif Tissue Int*. 1996;59(1):58–63.
- [17] Kim HM, Kim Y, Park SJ, et al. Thin film of low-crystalline calcium phosphate apatite formed at low temperature. *Biomaterials*. 2000;21(11):1129–1134.
- [18] Boissard CIR, Bourban PE, Tami AE, et al. Nanohydroxyapatite/poly(ester urethane) scaffold for bone tissue engineering. *Acta Biomater*. 2009;5(9):3316–3327.
- [19] Jayabalan M, Shalumon KT, Mitha MK, et al. Effect of hydroxyapatite on the biodegradation and biomechanical stability of polyester nanocomposites for orthopedic applications. *Acta Biomater*. 2010;6(3):763–775.
- [20] Hong Z, Zhang P, He C, et al. Nano-composite of poly(L-lactide) and surface grafted hydroxyapatite: mechanical properties and biocompatibility. *Biomaterials*. 2005;26(32):6296–6304.
- [21] Rezwan K, Chen QZ, Blaker JJ, et al. Biodegradable and bioactive porous polymer/inorganic composite scaffolds for bone tissue engineering. *Biomaterials*. 2006;27(18):3413–3331.
- [22] Bezwada RS, Jamiolkowski DD, Lee IY, et al. Monocryl suture, a new ultra-pliant absorbable monofilament suture. *Biomaterials*. 1995;16(15):1141–1148.
- [23] Khor HL, Ng KW, Htay AS, et al. Preliminary study of a polycaprolactone membrane utilized as epidermal substrate. *J Mater Sci Mater Med*. 2003;14(2):113–120.
- [24] Kim HW, Knowles JC, Kim HE. Development of hydroxyapatite bone scaffold for controlled drug release via poly(ϵ -caprolactone) and hydroxyapatite hybrid coating. *J Biomed Mater Res B Appl Biomater*. 2004;70(2):240–249.
- [25] Ural E, Kesenci K, Fambri L, et al. Poly(D,L-lactide/-caprolactone)/hydroxyapatite composites. *Biomaterials*. 2000;21(21):2147–2154.
- [26] Chrissafis K, Antoniadis G, Paraskevopoulos KM, et al. Comparative study of the effect of different nanoparticles on the mechanical properties and thermal degradation mechanism of in situ prepared poly(ϵ -caprolactone) nanocomposites. *Compos Sci Technol*. 2007;67(10):2165–2174.

- [27] Neuendorf RE, Saiz E, Tomsia AP, et al. Adhesion between biodegradable polymers and hydroxyapatite: relevance to synthetic bone-like materials and tissue engineering scaffolds. *Acta Biomater.* 2008;4(5):1288–1296.
- [28] Sanda F, Sanada H, Hibasaki Y, et al. Star polymer synthesis from ϵ -caprolactone utilizing polyol/protonic acid initiator. *Macromolecules.* 2002;35(3):680–683.
- [29] Dong CM, Qiu KY, Gu ZW, et al. Synthesis of star-shaped poly(ϵ -caprolactone)-b-poly(DL-lactic acid-alt-glycolic acid) with multifunctional initiator and stannous octoate catalyst. *Macromolecules.* 2001;34(14):4691–4696.
- [30] Mehmanchi M, Shokrollahi P, Atai M, et al. Supramolecular polycaprolactone nanocomposite based on functionalized hydroxyapatite. *J Bioact Comp Polym.* 2012;27(5):467–480.
- [31] Xiao Y, Lang S, Wang Y, et al. Effect of surface grafted hydroxyapatite on the improved performance of hydroxyapatite/poly(ϵ -caprolactone) scaffold. *Curr Nanosci.* 2014;10(6):855–862.
- [32] Cho YS, Cho Y-S, Gwak S-J. Fabrication of polycaprolactone/nano hydroxyapatite (PCL/nHA) 3D scaffold with enhanced in vitro cell response via design for additive manufacturing (DfAM). *Polymers.* 2021;13(9):1394–1312.
- [33] Mortazavian H, Picquet GA, Lejniaks J, et al. Understanding the role of shape and composition of star-shaped polymers and their ability to both bind and prevent bacteria attachment on oral relevant surfaces. *J Funct Biomater.* 2019;10:1–16.
- [34] Theiler S, Mela P, Diamantouros SE, et al. Fabrication of highly porous scaffolds for tissue engineering based on star-shaped functional poly(ϵ -caprolactone). *Biotechnol Bioeng.* 2011;108(3):694–703.
- [35] Landi E, Tampieri A, Celotti G, et al. Densification behaviour and mechanisms of synthetic hydroxyapatites. *J Eur Ceram Soc.* 2000;20(14–15):2377–2387.
- [36] Monmaturapoj N. Nano-size hydroxyapatite powders preparation by wet-chemical precipitation route. *J Metals Mater Min.* 2008;18:15–20.
- [37] Durrieu MC, Pallu S, Guillemot F, et al. Grafting RGD containing peptides onto hydroxyapatite to promote osteoblastic cells adhesion. *J Mater Sci Mater Med.* 2004;15(7):779–786.
- [38] Hunter WM, Greenwood FC. Preparation of iodine-131 labeled human growth hormone of high specific activity. *Nature.* 1962;194:495–498.
- [39] Stern HS, Zolle I, McAfee JG. Preparation of technetium (Tc^{99m})-labeled serum albumin (human). *Int J Appl Radiat Isotop.* 1965;16(4):283–288.
- [40] Mura-Galelli MJ, Voegel JC, Behr S, et al. Adsorption/desorption of human serum albumin on hydroxyapatite: a critical analysis of the Langmuir model. *Proc Natl Acad Sci USA.* 1991;88(13):5557–5561.
- [41] de Queiroz AAA, Barrak ER, Castro SC. Thermodynamic analysis of biomaterials. *J Mol Struct Theochem.* 1997;394(2-3):271–279.
- [42] International Organization for Standardization. Biological evaluation of medical devices. V. Tests for cytotoxicity: in vitro methods. ISO, editor. Vol. 10993-5. Geneva, Switzerland: International Organization for Standardization; 1999.
- [43] Gan Z, Fung JF, Jing X, et al. A novel laser light-scattering study of enzymatic biodegradation of poly(ϵ -caprolactone) nanoparticles. *Polymer.* 1999;40(8):1961–1967.
- [44] Leenslag JW, Pennings AJ. Synthesis of high-molecular-weight poly(L-lactide) initiated with tin 2-ethylhexanoate. *Makromol Chem.* 1987;188(8):1809–1814.
- [45] Valerio O, Pin JM, Misra M, et al. Synthesis of glycerol-based biopolyesters as toughness enhancers for polylactic acid bioplastic through reactive extrusion. *ACS Omega.* 2016;1(6):1284–1295.
- [46] Kowalski A, Duda A, Penczek S. Kinetics and mechanism of cyclic esters polymerization initiated with tin (II) octoate. 1. Polymerization of ϵ -caprolactone. *Macromol Rapid Commun.* 1998;19:567–572.

- [47] Lele BS, Leroux JC. Synthesis of novel amphiphilic star-shaped poly(ϵ -caprolactone)-block-poly(N-(2-hydroxypropyl)methacrylamide) by combination of ring-opening and chain transfer polymerization. *Polymer*. 2002;43(21):5595–5606.
- [48] Calderon M, Graeser R, Kratz F, et al. Development of enzymatically cleavable prodrugs derived from dendritic polyglycerol. *Bioorg Med Chem Lett*. 2009;19(14):3725–3728.
- [49] Zhang W, Zheng S, Guo Q. Synthesis and characterization of dendritic star-shaped poly(ϵ -caprolactone)-block-poly(L-lactide) block copolymers. *J. Appl Polym Sci*. 2007;106(1):417–424.
- [50] Londoño-Restrepo SM, Jeronimo-Cruz R, Millán-Malo BM, et al. Effect of the nano crystal size on the X-ray diffraction patterns of biogenic hydroxyapatite from human, bovine, and porcine bones. *Sci Rep*. 2019;9(1):1–12.
- [51] Ferraz MP, Monteiro FJ, Serro AP, et al. Effect of chemical composition on hydrophobicity and zeta potential of plasma sprayed HA/CaO-P₂O₅ glass coatings. *Biomaterials*. 2001;22(23):3105–3112.
- [52] Vandiver J, Dean D, Patel N, et al. Nanoscale variation in surface charge of synthetic hydroxyapatite detected by chemically and spatially specific high-resolution force spectroscopy. *Biomaterials*. 2005;26(3):271–283.
- [53] Weber N, Wendel HP, Kohn J. Formation of viscoelastic protein layers on polymeric surfaces relevant to platelet adhesion. *J Biomed Mater Res A*. 2005;72(4):420–427.
- [54] Vitte J, Benoliel AM, Pierres A, et al. Is there a predictable relationship between surface physical-chemical properties and cell behavior at the interface? *Eur Cell Mater*. 2004;7:52–63.
- [55] Johnson CA, Wu P, Lenhoff AM. Electrostatic and van der Waals contributions to protein adsorption: 2. Modeling of ordered arrays. *Langmuir*. 1994;10(10):3705–3713.
- [56] Sit PS, Marchant RE. Surface-dependent differences in fibrin assembly visualized by atomic force microscopy. *Surf Sci*. 2001;491(3):421–432.
- [57] Swain SK, Sarkar D. Study of BSA protein adsorption/release on hydroxyapatite nanoparticles. *Appl Surf Sci*. 2013;286:99–103.
- [58] Young BR, Pitt WG, Cooper SL. Protein adsorption on polymeric biomaterials: I. Adsorption isotherms. *J Colloid Interface Sci*. 1988;124(1):28–43.
- [59] Golander CG, Lin YS, Hlady V, et al. Wetting and plasma protein adsorption studies using surfaces with a hydrophobicity gradient. *Colloids Surf*. 1990;49:289–302.
- [60] Malmsten M. Ellipsometry studies of the effects of surface hydrophobicity on protein adsorption. *Colloids Surf B*. 1995;3(5):297–308.
- [61] Patil S, Sandberg A, Heckert E, et al. Protein adsorption and cellular uptake of cerium oxide nanoparticles as a function of zeta potential. *Biomaterials*. 2007;28(31):4600–4607.
- [62] Duracher D, Elaissari A, Mallet F, et al. Adsorption of modified HIV-1 capsid p24 protein onto thermosensitive and cationic core-shell poly(styrene)-poly(N-isopropylacrylamide) particles. *Langmuir*. 2000;16(23):9002–9008.
- [63] Prieto G, Sabín J, Ruso JM, et al. A study of the interaction between proteins and fully-fluorinated and fully-hydrogenated surfactants by ζ -potential measurements. *Colloids Surf A Phys Chem*. 2004;249(1–3):51–55.
- [64] Pitt CG, Gratzl MM, Kimmel GL, et al. Aliphatic polyesters. 2. The degradation of poly(D,L-lactide), poly(ϵ -caprolactone) and their copolymers in-vivo. *Biomaterials*. 1981;2(4):215–220.
- [65] Schmid RD, Verger R. Lipases: interfacial enzymes with attractive applications. *Angew Chem Int Ed Engl*. 1998;37(12):1608–1633.
- [66] Brzozowski AM, Savage H, Verma CS, et al. Structural origins of the interfacial activation in *Thermomyces (Humicola) lanuginosa* lipase. *Biochemistry*. 2000;39(49):15071–15082.
- [67] Miculescu F, Ciocan LT, Miculescu M, et al. Effect of heating process on microstructure level of cortical bone prepared for compositional analysis. *Dig J Nanomater Biostruct*. 2011;6:225–233.
- [68] Anselme K. Osteoblast adhesion on biomaterials. *Biomaterials*. 2000;21(7):667–681.

- [69] Anselme K, Bigerelle M, Noel B, et al. Qualitative and quantitative study of human osteoblast adhesion on materials with various surface roughnesses. *J Biomed Mater Res.* [2000](#);49(2):155–166.
- [70] Wei J, Yoshinari M, Takemoto S, et al. Adhesion of mouse fibroblasts on hexamethyldisiloxane surfaces with wide range of wettability. *J Biomed Mater Res B Appl Biomater.* [2007](#);81(1):66–75.
- [71] Wei J, Igarashi T, Okumori N, et al. Influence of surface wettability on competitive protein adsorption and initial attachment of osteoblasts. *Biomed Mater.* [2009](#);4:1–7.
- [72] Rickard DJ, Gowen M, MacDonald MR. Proliferative responses to estradiol, IL-1 alpha and TGF beta by cells expressing alkaline phosphatase in human osteoblast-like cell cultures. *Calcif Tissue Int.* [1993](#);52(3):227–233.
- [73] Chuenjitkuntaworn B, Inrung W, Damrongsri D, et al. Polycaprolactone/hydroxyapatite composite scaffolds: preparation, characterization, and in vitro and in vivo biological responses of human primary bone cells. *J Biomed Mater Res A.* [2010](#);94(1):241–251.